2013-01-01

Crystal Structure, Phase, And Optical Properties Of Yttrium-Doped Hafnium Oxide Nanocrystalline Thin Films

Alejandro Ortega
University of Texas at El Paso, ortegaach@gmail.com

CRYSTAL STRUCTURE, PHASE, AND OPTICAL PROPERTIES OF YTTRIUM-DOPED HAFNIUM OXIDE NANOCRYSTALLINE THIN FILMS

ALEJANDRO ORTEGA

Department of Metallurgical and Materials Engineering

APPROVED:

C.V. Ramana, Ph.D., Chair

David Roberson, Ph.D.

Stephen W. Stafford, Ph.D.

Benjamin C. Flores, Ph.D.
Dean of the Graduate School

By

Alejandro Ortega

2013

Dedication

To my parents, whose motivation led to the individual I conform right now, and the one I am yet to be. I owe them my existence and decades of dedication, patience and hard work. This piece of work is the smallest detail I can do for the love I feel for them.

CRYSTAL STRUCTURE, PHASE, AND OPTICAL PROPERTIES OF YTTRIUM-DOPED HAFNIUM OXIDE NANOCRYSTALLINE THIN FILMS

By

ALEJANDRO ORTEGA, B.S. Mechanical Engineering

THESIS

Presented to the Faculty of the Graduate School of
The University of Texas at El Paso
in Partial Fulfillment
of the Requirements
for the Degree of

MASTER OF SCIENCE

Department of Metallurgical & Materials Engineering
THE UNIVERSITY OF TEXAS AT EL PASO
December 2013

Acknowledgements

I would like to thank my thesis advisor and mentor, Dr. Ramana for his hard work and dedication on this cause. I appreciate his patience in transmitting us his knowledge, his assistance in written reports and all types of support he provided. I recognize him not only as a great mentor, but as an even greater individual. I also want to acknowledge Dr. Ramana's research team for supporting me in uncountable occasions with unconditional help. I also want to thank UTEP for providing me this opportunity, with special mention to the department of Metallurgical & Materials Engineering for educating me throughout my master's and providing faculty with vast experience in their fields. Special thanks to Dr. Noveron for aiding me in my life and research endeavors.

Table of Contents

List of Tables

List of Figures

CHAPTER 1: Introduction

On April 1965, Gordon Moore published a paper stating that "the amount of transistors in the integrated circuits would be doubled every two years," leading an exponential growth of transistors over time [1]. Until now, this prediction has proven to be not only true, but also precise. Back in the 1970's, integrated circuits contained a few thousand transistors. Now in 2013, each chip may contain up to several billion MOSFETs (metal-oxide semiconductor field effect transistors) ranging in the size of a few dozen nanometers. This decrease in size leads to faster computing power and improved functionality of an integrated circuit, leading to an exponential growth of the semiconductor market, also opening the opportunity to research in materials and electronics [2,3]. In other words, the idea is to build smaller transistors, leading to a better performance, a market growth and more investment, which is then used to research on even smaller pieces, making a virtuous cycle. Perhaps the only challenge is to make a mass scale production of these integrated circuits, but corporations have managed to solve this problem with etching and other specialized techniques as the demand of more powerful computing market grows.

However, Moore's law faces a limit in terms of transistor thickness. Silicon dioxide (SiO_2) is the most widely used and well known gate dielectric for MOSFETs [1,2,4]. SiO_2 is cheap, abundant and easy to manufacture. It has been

used for decades and its lattice defects have been extensively studied. However, gate current leakage is a serious concern, and due to this problem Moore's law will reach the limit as transistors get smaller and smaller [3]. Thinner SiO_2 based transistors experience a phenomenon called quantum tunneling (which originates gate current leakage) and it starts being noticeable at approximately 15 nm, below which tunneling increases exponentially [4]. The current drains due to the electrons in the valence band that tunnel to the conduction band, leaving holes behind which later diffuse into the substrate. In other words, tunneling is a major constraint in the design when oxide thickness gets very small and a considerable amount of current leakage could cause complete circuit failure [5]. This is due to the fact that silicon dioxide, although has a wide band gap (~9 eV), its dielectric constant is relatively low (~4), thus being unable to store greater amounts of electrical energy as compared to other materials [6]. All these factors have led to intense research on new alternative materials that can be produced in smaller scales, have a stable metal-oxide interface, a wide band gap and higher dielectric constant than that of SiO_2. Direct tunneling, J_{DT} may be expressed as follows:

$$\boldsymbol{J_{DT} \propto \exp\left(-\frac{1}{\hbar}\sqrt{8m^{*}\Phi_b T_{OX}}\right)} \qquad [1.1]$$

where ħ is Planck's constant, m^* is the effective mass, $\boldsymbol{\Phi_b}$ is the energy band discontinuity and T_{OX} is the thickness of the oxide. $\boldsymbol{\Phi_b}$, k and m^* are a determining factor for reducing the leakage current. T_{OX} can be expressed by:

$$\mathbf{T_{ox}} = \frac{\boldsymbol{k}}{\boldsymbol{k_{SiO2}}} \boldsymbol{EOT} \qquad [\mathbf{1.2}]$$

where EOT is the equivalent oxide thickness. Several materials have been studied as potential replacements for SiO_2. Such materials must exhibit a wide energy gap. The material options include metal oxides and nitrides, with two or even three dopants to suitably tune the properties. Some examples of these oxides include crystalline and amorphous tantalum oxide (Ta_2O_5), barium-strontium doped titanium oxide ($[Ba_xSr_{1-x}]TiO_3$), lanthanum aluminate ($LaAlO_3$), lithium niobiate ($LiNbO_3$), gadolinium scandanate ($GdScO_3$), samarium scandanate ($SmScO_3$), lead zirconate titanate ($Pb[Zr,Ti]O_3$), zirconium oxide (ZrO_2), hafnium oxide (HfO_2), among others [7-10]. In order to have an ideal metal-oxide interface, all of these materials must be thermodynamically stable at about 900-1000 °C, the range of temperatures at which the integrated circuits are processed [7,10]. If this condition is not met, these interfaces could lower the dielectric constant of the whole system and causes the property/performance degradation. Thus, care must be taken when studying an ideal replacement for SiO_2, also involving other variables such as deposition method, point defects, grain boundaries and crystal structure. The comprehension of all these factors is crucial towards a proper design for smaller, stable and functional MOSFETs.

1.1 Hafnium Oxide

Hafnium oxide (HfO_2, familiar to the community as 'Hafnia') a is a versatile oxide material with potential electronic and optoelectronic applications [9,10]. In addition, its high melting point (~2760 °C) and its ability to block UV radiation make it an ideal candidate for heat windows and sensors operating at high temperatures [10,11]. However, HfO_2 oxide faces a few major problems, such as mineral scarcity in the earth's crust, high extraction costs, and the high temperature required to stabilize the cubic phase (~2600 °C). Since the cubic phase exhibits a greater relative permittivity, the latter is a major constraint for integrated circuit design [12].

The arrangement of oxygen atoms is the major factor that determines the tetragonal to cubic phase transformation in hafnia. In the tetragonal phase the oxygen atoms are slightly displaced from the [001] plane [13]. Terki et al showed using a DFT simulation that two different charges exists in the same plane in the tetragonal phase, due to two different distances between the oxygen bonds [13].

1.2 Yttrium-Doped Hafnium Oxide

The focus of the present work is towards the structural and optical properties of yttrium(Y)-doped hafnium oxide (HfO_2), which is referred to YDH throughout this thesis. YDH exhibits outstanding chemical stability, large band gap, thermodynamical stability, optical and electrical properties.

Yttrium-doped hafnia exhibits a relatively wide range of properties throughout its different phases, depending on the film thickness, yttrium concentration, substrate temperature and materials, deposition method and fabrication conditions [12]. For instance, the relative permittivity (k) was shown both theoretically and experimentally to attain significantly higher values in the cubic phase (~29) compared to monoclinic phase (~16-18)[14,15]. In addition to its electrical properties, YDH has a great potential for thermal barrier coating applications, thanks to its high melting point and thermal properties in general [12]. The present work is intended to study the crystal structure, phase and optical properties of YDH nanocrystalline films as function of variable growth conditions and to determine the effect of annealing on structure and properties.

1.3 Materials comparison

Table 1 lists the band gap (E_g), dielectric constant (relative permittivity), refractive index (n), thermal conductivity (k), density (ρ), melting point (T_m) and crystal structure of several substances belonging to various groups. They are arranged according to their band gaps, from lowest to highest. The melting points of the complex oxides are clearly higher than any other group, with other semiconductors and oxides having also high T_m. The band gap of complex oxides tends to be high, although there are just a few listed, with the smallest gaps in the non-oxide ceramics and pure elements. Refractive indices tend to be higher in pure elements, probably due to the high interaction between the

heavy packed electrons and the photons, although some non-oxide ceramics light seems to struggle as it passes through. In the case of thermal conductivity, and somewhat obvious, the more complex the material, the harder it is for the energy to be transferred between their atoms.

Table 1. Band gap (E_g), dielectric constant (k), refractive index (n), thermal conductivity (λ), density (ρ), melting point (T_m) and crystal structure of common substances, at a wavelength of approximately 650 - 530nm and room temperature [16-29].

Material	E_g (eV)	K	n	λ ($\frac{W}{mK}$)	ρ ($\frac{g}{cm^3}$)	T_m (K)	Crystal Structure
Vacuum	-	1	1	-	-	-	-
Common substances							
Air	-	~1	~1	0.026	~0.0012	-	Gas
Ammonia	-	17	1.33	0.022	0.73	195	Liquid
Benzene	-	2	1.50	0.16	0.877	279	Liquid
Methanol	-	30	1.33	0.21	0.792	176	Liquid
Sulfuric Acid	-	100	1.41	0.26	1.84	283	Liquid
Water	-	80	1.33	0.59	1	273	Liquid
Pure elements							
Al	0	4.2	1.39	237	2.70	933	FCC
Au	0	0.236	1.47	318	19.30	1337	FCC
Te	0.33	n/a	4.93	1.97-3.38	6.24	723	Hexagonal
Ge	0.66	16	5.48	60	5.232	1211	Diamond cubic
Si	1.11	11-12	3.96	149	2.329	1687	Diamond cubic
Se (Grey)	1.74	6.1-7.4	2.79	0.519	4.81	494	Hexagonal
C (Diamond)	5.5	5.5-10	2.42	900-2320	3.53	3823	Diamond cubic
Translucid Materials (IR-Vis)							
Calcite ($CaCO_3$)	n/a	8	1.66	1.3	2.711	1098	Trigonal
Spinel ($MgAl_2O_4$)	n/a	8.2	1.64	15	3.58	2408	Cubic
ITO (In_2O_3 - SnO_2)	4.21	7.6	1.99	10	7.160	1800-2200	Amorphous
GeO_2	5.54	18	1.65	60	4.228	1388	Hexagonal
Al_2O_3	7.3	9-11.5	1.77	30	3.95	2345	Polymorph
NaCl	8.97	3–15	1.54	3.5-4.8	2.165	1074	Cubic
SiO_2	9	3-5	1.46	1.4-3	2.648	1600-1725	Polymorph
Ceramics: oxide semiconductors							
WO_3	2.8	2.2	2.0	1.6	7.16	1746	Monoclinic
TiO_2 (Rutile)	3.0	173	2.49	13	4.23	2116	Tetragonal
ZnO	3.2	1.7	2.4	21	5.606	2248	Wurtzite
Ga_2O_3	4.54	10	1.92	n/a	5.88	1998	Tetragonal
Zirconia (ZrO_2)	4.99	12.5	2.18	3	5.68	2998	Cubic
Yttria (Y_2O_3)	5.6	12	1.86	27	5.010	2698	Cubic
HfO_2	5.9	18-20	1.91	23	9.68	3031	Monoclinic

Material	E_g (eV)	K	n	λ ($\frac{W}{mK}$)	ρ ($\frac{g}{cm^3}$)	T_m (K)	Crystal Structure
Ceramics: complex oxides							
YVO_4	n/a	12	1.99	5.2	4.24	2083	Zinc tetragonal
$SrTiO_3$	3.3	310	2.41	12	5.11	2353	Perovskite
YSZ	4.2-4.96	23-30	2.05	2-3	6.10	2700-2900	Cubic
YDH	5.4-6.04	24-27	2.02	0.89	8.71	3051	Cubic
Ceramics: other semiconductors							
GaAs	1.43	12.5	3.93	55	5.318	1511	Zinc blende
AlAs	2.16	13	3.07	90	3.72	2013	Zinc blende
GaP	2.26	9	3.02	11	4.138	1750	Zinc blende
AgBr	2.5	12.2	2.23	1.2	6.473	705	FCC
SiC	2.86	10.8	2.55	36	3.21	3003	Zinc blende
CuCl	3.31	20	1.96	n/a	4.145	703	Zinc blende
ZnS	3.6	8.2	2.36	27	4.090	1458	Wurtzite
KI	6.17	5.6	1.63	2.1	3.126	954	FCC
AlN	6.28	9.1	2.05	285	1.9	2473	Wurtzite
MgF_2	10.8	5.5	1.35	21	3.148	1536	Tetragonal

1.4 Crystal structure

Hafnium oxide exhibits various polymorphs; monoclinic (M), tetragonal (T) and cubic (C) [12,13]. Monoclinic structure of HfO_2 is the most thermodynamically stable phase under normal temperature and pressure conditions. At temperatures higher than 1700 °C, HfO_2 transforms to tetragonal phase. Transformation to cubic polymorph having the fluorite structure occurs at 2600 °C [30].

1.4.1 Phase stabilization

Similar to zirconia (ZrO_2), doping a small amount of yttria (Y_2O_3) stabilizes the HfO_2 cubic phase (Fm3m space group) [31,32]. Doping of Y_2O_3 into HfO_2 replaces Hf^{4+} ions in lattice with the Y^{3+} ions which induce the replacement of

three O^{2-} ions into four O^{2-} ions, producing oxygen vacancies [33]. The overall cubic symmetry of HfO_2 is, then, preserved down to room temperature in yttria-doped hafnia (YDH), which belongs to the group of fluorite-structured (CaF2) [30] oxygen superionic conductors. In addition, transformation of the monoclinic hafnia to the cubic YDH structure is expected to be stable due to the difference between surface energies of the crystal structures and high symmetry [34]. The phase diagram of YDH system is shown in Figure 1.

The doping of Y_2O_3 replaces Hf^{4+} ions in the hafnia lattice with the Y^{3+} ions, this triggers the replacement of three O^{2-} ions into four O^{2-} ions, producing oxygen vacancies [34]. These oxygen vacancies, V^{2+}, are potential acceptors for electrons. The annealing of the YDH thin films increases the diffusion of oxygen into the lattice, introducing more electrons, finally filling up the vacancies with electrons acting as self-trapped polarons inside them, changing the vacancy charge. These point defects can accept up to four electrons (V^{2+}, V^{+}, V^{0}, V^{-}, V^{2-}). Adding one electron into the V^{2+} vacancy polarizes the lattice and shifts the defect level by about 2 eV. Balancing the charge to V^{0} causes the ions to occupy its perfect lattice sites. The addition of two extra electrons (V^{-}, V^{-2}) polarizes the lattice even more and another localized gap emerges from the conduction band minimum. This data was collected using electron density functional theory [4-6].

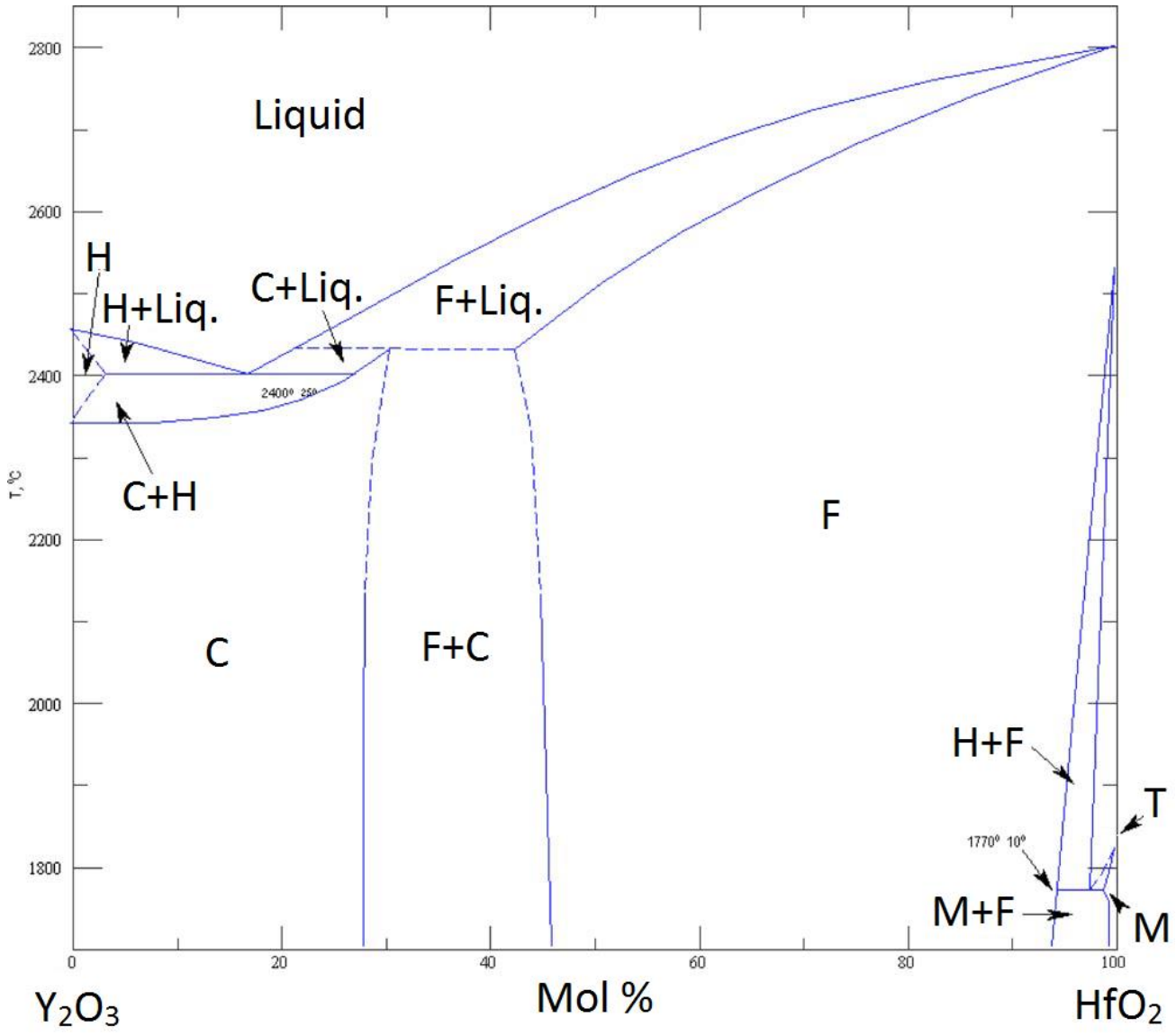

Figure 1. Phase diagram of the Yttria-Hafnia system [59].

1.5 Optical properties

The optical properties of a semiconductor are determined by the interaction of the electromagnetic radiation with the material, especially with the electrons. This interaction produces the absorption, reflection, emission and scattering of photons by the atoms of the material. Optical techniques are non-destructive and the alteration that the photons do to the materials' internal structure is negligible. There are a wide variety of methods available for thin film characterization, such as ellipsometry, optical absorption, optical microscopy, etc. All the optical properties discussed in this thesis were obtained by optical spectroscopy ranging from the near-infrared to the ultraviolet spectrum.

Understanding the optical properties of the hafnia system is crucial and of significant attention for research by the scientific community. The optical properties of pure hafnia and YDH reported in the literature are compared in Figures 2 and 3 below. All YDH films show interference fringes (Fig. 2) in the near infrared and visible light spectrum, descending in a steep slope as soon as the photon wavelength reaches the ultraviolet region at around 250 nm. This sudden absorption phenomenon occurs due to the electrons of the valence band jumping to the conduction band with the ultraviolet light providing the necessary energy to overcome the energy gap between the valence band and the conduction band. This energy gap is also known as the band gap.

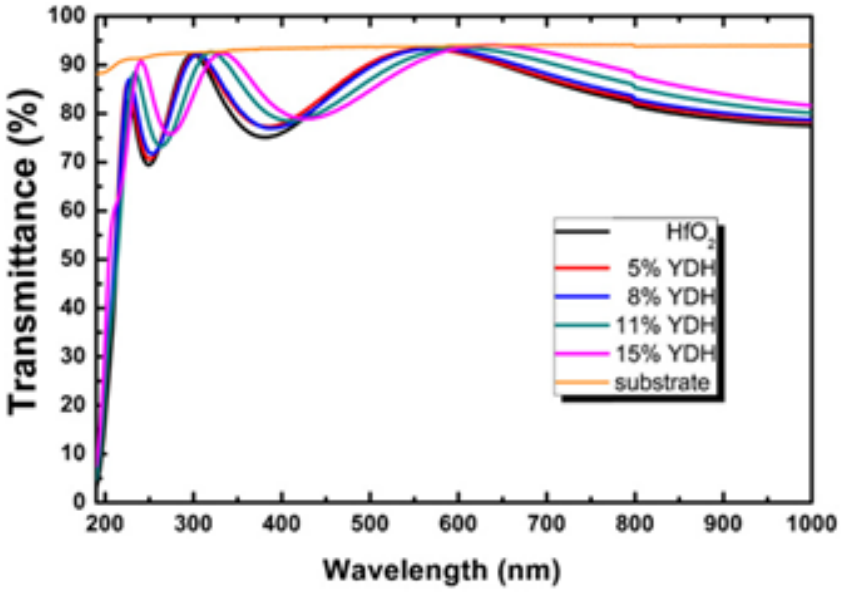

Figure 1. Transmittance spectra of YDH films with an average thickness of 150nm. Measurements performed by Chen *et al*., *App. Sur. Sci.*, 271 248-252 (2013).

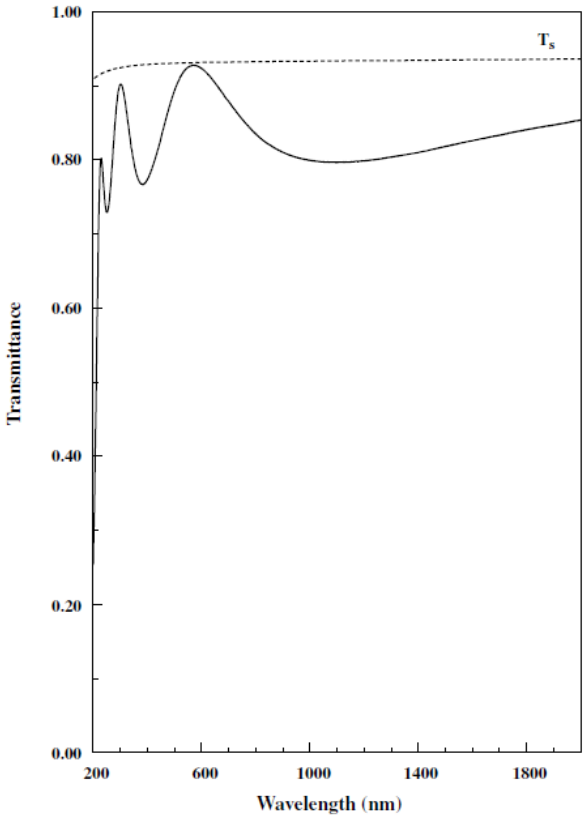

Figure 2 Transmittance spectra for monoclinic HfO_2 with a thickness of 145 nm. Measurements performed by Al-Kuhaili, *Opt. Matls.,* 27 385 (2004).

1.5.1 Absorption coefficient

The absorption coefficient (α) is a measure of how the ability of light to penetrate a given material (although phonons and other particles can be measured using this quantity too) and its units are 1/cm. It is dependent on the absorbed light at a given wavelength and the thickness of the sample:

$$\boldsymbol{I = I_0 \exp(-\alpha d)} \qquad [1.3]$$

where I is the transmitted light intensity, I_0 is an incident light intensity and d is the thickness. The transmittance ratio is given by:

$$\boldsymbol{T = \frac{I}{I_0}} \qquad [1.4]$$

So the equation can be simplified to:

$$\boldsymbol{\alpha = -\frac{1}{d} Ln(T) = \frac{4\pi k_e}{\lambda}} \qquad [1.5]$$

This logically implies that the absorption coefficient varies at different photon energies (smaller light wavelengths have higher photon energies). The absorption coefficient for a given photon energy is proportional for a transition from its initial state to its final state and the density of the electrons present in the first state and the density of empty states in the excited states. Ideally, below the energy gap the absorption coefficient tends to zero [64].

1.5.2 Band gap

The band gap (also called energy gap, E_g) is the region of an atom in a solid material represented by an energy range in the electronic band structure where no electrons can exist [15]. In theory, it is the energy difference between the top of the valence band and the bottom of the conduction band and it is the cause of splitting these two. The interaction between phonons and photons with electrons carries a momentum, and the transferred energy must be conserved. This energy momentum can be obtained by solving the Schrödinger equation for one electron.

The band gap, E_g, can obtained following the absorption power law defined as:

$$\boldsymbol{\alpha}\hbar\boldsymbol{\nu} = \boldsymbol{B}(\hbar\boldsymbol{\nu} - \boldsymbol{E_g})^{\boldsymbol{n}} \quad [1.6]$$

where $\boldsymbol{\alpha}$ is the absorption coefficient, $\hbar\boldsymbol{\nu}$ is the incident photon energy, B is the absorption edge parameter and n is an exponent, dependent on whether the band gap is direct allowed, direct forbidden or indirect.

1.5.3 Refractive index and dielectric constant

The index of refraction (n) is a dimensionless number that measures by how much the light is slowed down by a medium,

$$\tilde{n} = \boldsymbol{n_r} - \boldsymbol{ik} \quad [\mathbf{1.7}]$$

The real part of the refractive index, n_r, describes how light propagates through the medium. It is a ratio between the speed of light in vacuum (c) and the speed of light in that substance (v), given by:

$$\boldsymbol{n_r = \frac{c}{v} = \frac{\lambda_0}{\lambda}} \qquad [1.8]$$

The imaginary part or the extinction coefficient, k_e, determines the light that has been absorbed by the material. The index of refraction is a function of wavelength, and can be derived from the electromagnetic wave equations, which are derived from Maxwell's equations.

On the other hand the dielectric constant, k, is the amount of electrical energy that a material can store divided by an applied voltage, as compared to that stored in a vacuum, and it is directly related to the refractive index. It can be defined in many ways but most essential form is:

$$\boldsymbol{k = \frac{\epsilon(w)}{\epsilon_0}} \qquad [1.9]$$

where $\boldsymbol{\epsilon}$(w) is the absolute permittivity of the material dependent on the frequency and $\boldsymbol{\epsilon_0}$ is the permittivity of vacuum. Table 1 lists the refractive index and dielectric constant of various materials.

1.5.4 Diffusion of oxygen into hafnia

Foster *et al* [17] performed DFT calculations of pure hafnia samples, concluding that oxygen incorporates in both atomic and molecular form, but

the atomic form predominates, similar to zirconia [18,19]. The addition of oxygen into the lattice may deeply change the electrical properties of a semiconductor; it may generate undesired silica-hafnia interfaces and introduces point defects. The mechanism of oxygen diffusion in ceramics can be classified as exchange or interstitial process. Exchange (also known as intersticialcy) consists in the continuous replacement of the atom lattice site by diffusion, so the lattice site itself can then diffuse. On the other hand, diffusion by interstitials requires the atom to travel longer distances between the lattice sites, relaxing the stress in the lattice and making it more difficult for the bond with a lattice site. Adding two electrons into the hafnia lattice creates a complete outer shell, allowing oxygen to be stable in the crystal. Foster *et al* conclude that the oxygen defects are only stable in the hafnia lattice as ions and that, as this process takes place, atoms undergo relaxation across the diffusion path.

1.5.5 Diffusion of oxygen into yttria stabilized hafnia

In the particular case of YDH, the annealing of the thin films increases the diffusion of oxygen into the lattice, introducing more electrons, finally filling up the vacancies produced by yttria (discussed in section (1.1.1) with electrons acting as self-trapped polarons inside them, changing the vacancy charge. These point defects can accept up to four electrons (V^{2+}, V^{+}, V^{0}, V^{-}, V^{2-}). Adding one electron into the V^{2+} vacancy polarizes the lattice and shifts the defect level by about 2eV. Balancing the charge to V^{0} causes the ions to occupy its perfect

lattice sites. The addition of two extra electrons (V^{-}, V^{-2}) polarizes the lattice even more and another localized gap emerges from the conduction band minimum. This data was collected with electron density functional theory calculations [17,19-23].

CHAPTER 2: Methodology

2.1 Experimental procedures

Yttrium-doped hafnium oxide (YDH) thin films were deposited onto silicon (Si) (100) wafers, sapphire (Al_2O_3) and optical grade quartz substrates by radio-frequency magnetron sputtering. All the substrates were thoroughly cleaned and dried with nitrogen before introducing them into the vacuum chamber, which was initially evacuated to a base pressure of ~0.21 mPa. YDH target (5 cm diameter, 0.32 cm thick) (Plasmaterials Inc.) was used for sputtering. The content of yttria in YDH target was maintained at 7.5 mol% (7.5 YDH). The YDH target was placed on a sputter gun, which was correspondingly placed at a distance of 8 cm from the substrate. Sputtering was performed at a pressure of 0.2 Pa. A sputtering power of 30 W was initially applied to the target while introducing high purity argon (Ar) into the chamber causing plasma ignition. Once ignited, the power was increased to 80 W to deposit the films. The Ar gas flow (20 sccm) was controlled using 6 MKS mass flow meters. Before each deposition, the YDH-target was pre-sputtered for 10 minutes using Ar keeping the shutter above the gun closed. Deposition was made under variable deposition time to obtain films with a thickness (d_{YDH}) ranging from ~25 nm to ~1100 nm (or 1.1μm).

The substrates were heated by halogen lamps and the desired temperature was controlled by Athena X25 controller. X-ray diffraction (XRD) measurements were performed using a Bruker D8 Advance x-ray diffractometer.

All the measurements were made ex-situ as a function of T_s. XRD patterns were recorded using CuKα radiation (λ=1.54056 Å) at RT. Surface imaging analysis was performed using a high-performance and ultra-high resolution scanning electron microscope (Hitachi S-4800). The secondary electron imaging was performed on YDH films grown on Si wafers using carbon paste at the ends to avoid charging problems. In addition, Optical properties of the YDH films were evaluated using spectrophotometric optical transmission and reflectance measurements using Cary 5000 UV-VIS-NIR double-beam spectrophotometer. Films grown on optical grade quartz substrates were employed for optical property measurements.

2.2 Sputter deposition

Sputtering is a physical process whereby atoms are ejected from a solid surface through the mechanism of friction caused by ions traveling at high energies. The momentum is exchanged between the particles and it must be conserved, so if this energy surpasses the bond energy between the bombarded atom and the neighboring molecules, it will fly away from the solid. The gun, which generates ions in a radio frequency glow discharge, is placed in front of the target [51].

All the samples discussed in this paper were deposited by magnetron sputtering, a process that releases ionized argon and the target has a magnetic field configured parallel to it.

2.3 Samples and deposition parameters

Four sets of samples were prepared: one batch consisting on five samples was deposited on quartz and silicon at variable deposition times (30 min – 6 hr). These samples were sputtered at a fixed substrate temperature (T_s) of 400 °C, which was found to be the optimum to produce good crystalline films with grain size in nanoscale dimensions [56,57]. Furthermore, variable deposition time produces the films with variable thickness. Also, in order to maintain the constant deposition rate, the sputtering power was kept constant at 80 W. The deposition conditions for this set of samples were listed below.

Table 2. Deposition parameter for YDH sputtered at 400°C.

Deposition Time	Deposition Temp.(°C)	Thickness (nm)
30 min	400	29
1 hr	400	51
2 hr	400	219
4 hr	400	630
6 hr	400	1074

The second set nine samples deposited at various temperatures for a constant time of deposition (1.5 hours). The sputtering power was kept at 80 W. These samples were further annealed into two categories: samples annealed at a fixed temperature and samples annealed at a fixed time, as shown in Tables 3 and 4, respectively.

Table 3. Deposition parameters for YDH annealed for 12 hours, varying temperature.

Deposition Time	Deposition Temp. (°C)	Annealing Temp. (°C)	Annealing Time (hr)	Thickness (nm)
1.5 hr	500	1100	12	454
1.5 hr	400	1200	12	416
1.5 hr	500	1300	12	374
1.5 hr	400	1400	12	481
1.5 hr	500	1500	12	443

Table 4. Deposition parameters for YDH annealed at a fixed temperature (1300°C), varying time.

Deposition Time	Deposition Temp. (°C)	Annealing Temp. (°C)	Annealing Time (hr)	Thickness (nm)
1.5 hr	500	1300	3	476
1.5 hr	200	1300	6	538
1.5 hr	400	1300	9	525
1.5 hr	500	1300	12	374
1.5 hr	300	1300	24	547

2.4 Thickness calculation

The thickness of each sample was calculated by using only the transmittance spectra. In addition, thickness values were verified by profilometry. In optical spectra, by selecting a fringe, its adjacent maximum and minimum, the thickness can be calculated. This method was developed by Rhino Swanepoel in 1983, performed on silicon thin films. Swanepoel's method is widely accepted as a reliable way to find the thickness of a thin film [32,33]. While the method can be quite complex due to error corrections and other optical factors, it can be fairly approximated to the following equation:

$$\boldsymbol{d = \frac{\lambda_M \lambda_m}{2(\lambda_M - \lambda_m)}} \quad [2.1]$$

where d is the thickness (usually in nanometers), λ_M is the photon wavelength at the adjacent maxima and λ_m at the adjacent minima. Care must be taken while choosing the points of the maximum and minimum, otherwise it can yield errors up to 100%. The thicknesses of the films studied by the present work were determined using Swanepoel's method, and few of them correlated with ellipsometry (samples grown at fixed temperature and varying times). In the present work, thickness is referred to d_{YDH}.

2.5 Absorption coefficient, bandgap and index of refraction

The absorption coefficient and Bandgap were as well calculated by using the transmittance spectra given by the UV-Cary spectrophotometer. The absorption coefficient, $\boldsymbol{\alpha}$(cm^{-1}), as discussed on section 1.3.1 and 1.3.2, is obtained with the following formula:

$$\boldsymbol{\alpha = -\frac{1}{d} Ln(T)} \quad [2.2]$$

The thickness, d, is calculated with Swanepoel's method, discussed in the section above 2.2 [32,33].

The bandgap was calculated using the following formula:

$$y = (\alpha E_p)^2 \quad [2.3]$$

The y stands for the y axis, α is the absorption coefficient and E_p the photon energy. The whole equation is square due to the nature of hafnia to have a direct allowed bandgap, as explained in section 1.3.2. Both α and E_g were calculated using the transmittance spectra in an excel spreadsheet.

The index of refraction, n, was also calculated using a method developed by Rhino Swanepoel using only the transmittance spectra using the following formula [32,33]:

$$M = \frac{2s}{T_m} - \frac{s^2 + 1}{2} \qquad [2.4]$$

and

$$n = \sqrt{M + \sqrt{(M^2 - s^2)}} \qquad [2.5]$$

where M is a constant, s is the wafer's index of refraction (1.54 for quartz, assumed to be constant), and T_m is the minima of the interference fringes.

CHAPTER 3: Phase Analysis

3.1 Surface morphology and cross sectional analysis

The surface morphology of YDH films is shown in Fig. 4a and b for variable d_{YDH}. It is evident from the SEM images that the d_{YDH} plays an important role in the growth and distribution characteristics of the grains. It is evident that the morphology of all the YDH films is characterized by the dense grains; however, the surface morphology evolves into different shape and size with increasing d_{YDH}. At d_{YDH} = 26–70 nm (Fig. 4a), the surface is characterized by small, dense granular morphology, characteristic of the M-YDH phase. The surface morphology of M-YDH films in this work is in good agreement with that observed for pure, monoclinic HfO_2 films grown by sputter-deposition [56]. Increasing d_{YDH} induces a change in the morphology where the grains grown in size along with a change in shape. All the grains are not equally grown or similarly distributed. Specific particles are circled in SEM micrograph of d_{YDH} = 70 nm sample where the particles seem to be nucleating differently compared those observed common and for M-YDH films. Based on XRD results coupled with morphology observations, we believe that these are characteristic of C-YDH phase. The SEM images of YDH films with d_{YDH} = 190 nm (Fig. 4b) indicate the characteristic morphology as noted for cubic phase YDH films [57]. This observation coupled with XRD studies indicate that the increasing d_{YDH} to 350 nm results in the formation of fully C-YDH phase. No appreciable changes are noted with further increase in d_{YDH} up to 750 nm, at which point agglomeration of grains occurred

as noted in SEM micrograph (Fig. 4b) of sample with d_{YDH} = 1100 nm. These C-YDH films were noted to be exhibiting (002) texturing as seen in XRD studies. The observed results in XRD and SEM, specifically the nature of phase and the transformations can be understood based on the effect of three important parameters: (1) the crystallite size and surface/interface energy, (2) the dopant chemistry and concentration, and (3) stress-induced during film growth, which in turn dependent on the processing conditions. These parameters were able account for the structure, phase and properties of pure and doped HfO_2 films in the literature [61]. In the present case, Y-doping concentration is not quite sufficient in the early stages of growth to produce the C-YDH films. However, progressive increase in thickness accounts for the overall Y-dopant concentration and, therefore, M–C phase transformation occurs. The interface morphology of YDH films is shown in Fig. 4c. The cross-sectional SEM images of representative samples corresponding to M-phase and C-phase are shown. The important observations that can be derived from cross-sectional SEM micrographs are the following. All of the YDH films exhibit dense, columnar structure, which is the characteristic of HfO_2-based thin films and coatings [56]. However, it can be noted that the width of the columnar grains increases with increasing d_{YDH}. Perhaps, the grains are growing laterally while the additional YDH layers are growing in a normal direction on the substrate surface with continue deposition. Such growth mechanism favors the columnar width of the grains to increase as a function of d_{YDH}.

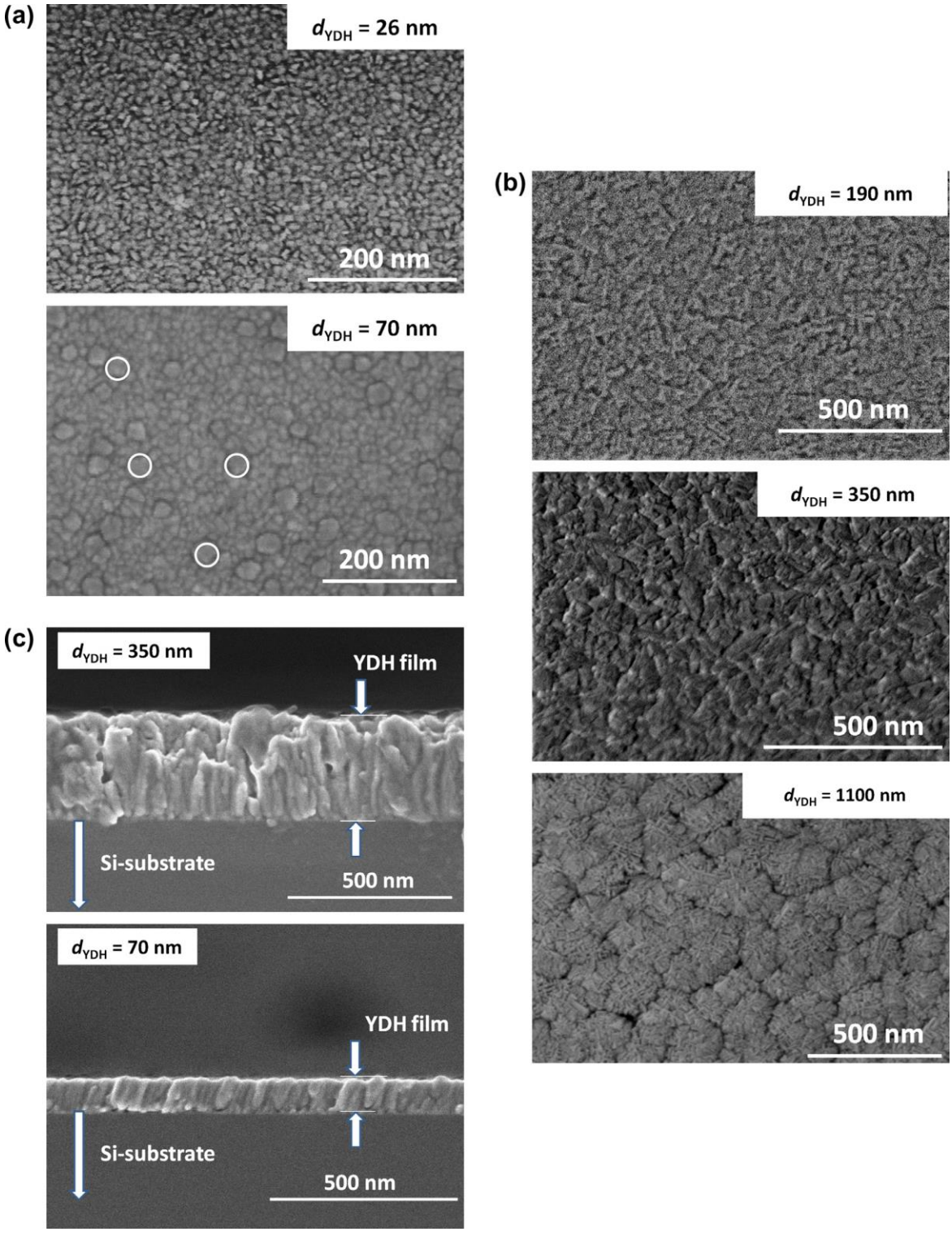

Figure 4. SEM images of representative YDH films as a function of thickness. The d_{YDH} values are as indicated in the SEM micrographs. (a) SEM images of relatively thin YDH films. (b) SEM images of relatively thicker YDH films. (c) Cross-section SEM images of representative YDH films highlighting their interface structure and morphology. Dense, columnar structure is evident in the micrographs.

3.2 Cubic and monoclinic phases as a function of thickness

The XRD patterns are compared in two ways: samples as a function of thickness (Figures 5 and 6) and as a function of deposition time and annealing temperature (Figures 7 and 8). Figure 5 exhibits a predominant monoclinic structure, with high peaks in the plane (-111), at about 2θ of 27.5°. Planes (022) and (113) are also present as the samples get thicker, at about 70nm, where the cubic structure starts to form. At 200nm the cubic structure becomes noticeable in samples with greater thickness; these planes present a stronger evidence of the cubic structure [31]. In addition, some 27.5° peaks in the low thickness samples are broad and finally narrow down as the thickness increases, suggesting that there is some degree of amorphous structure in the thinner films that disappears as the films stabilizes into the cubic structure [60]. The samples with a thickness greater than 750 nm become predominantly cubic and seem to be stable, with little or no evidence of amorphous regions or monoclinic phase.

In addition, the peak at 27.5° evolves to 28.1° as the thickness increases, suggesting that the lattice was originally strained in samples with lower thicknesses. This is yet more evidence indicating that the structure is stabilized as the films become thick (at about 200 nm).

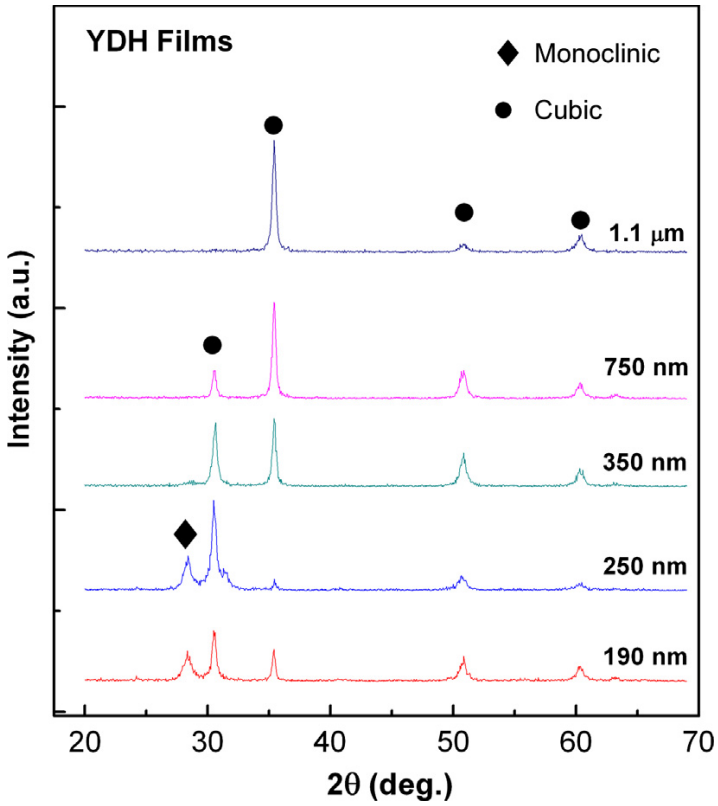

Figure 3 XRD patterns of YDH films with d_{YDH} 200 nm. The YDH films exhibit the phase.

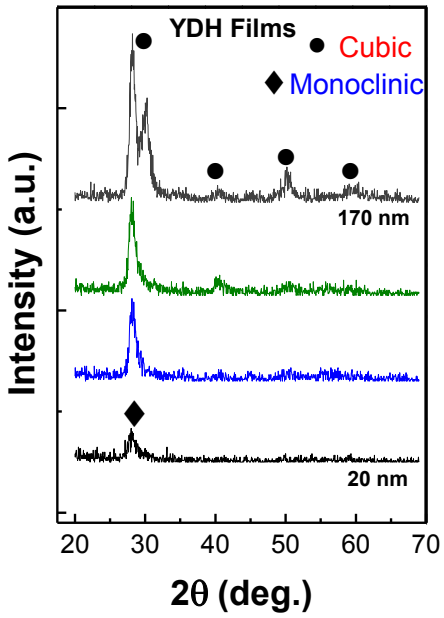

Figure 4 XRD patterns of YDH films with d_{YDH} < 200 nm. The YDH films exhibit the phase as indicated. All the films are predominantly monoclinic.

3.3 Cubic and monoclinic phases as a function of time and temperature

The other XRD comparison is as a function of deposition time and annealing temperature. The sample deposited for just 30 min exhibits a small portion of the monoclinic phase, exhibiting the well-known monoclinic peak (-111) at 27.5°, but it is predominantly amorphous and relatively thin, with a thickness of 29 nm. The samples deposited for 1 and 2 hours (thickness of 51 and 217 nm, respectively) start exhibiting the cubic phase, although the sample deposited for two hours still has traces of monoclinic regions, as discussed on the previous section. The sample deposited for six hours is all cubic and stable.

The samples annealed as a function of temperature are more complex than the rest of the samples. This is due to the fact that other elements get diffused into the lattice (mainly oxygen and nitrogen), changing the refracting planes and the optical properties in general. How this diffusion process of electron carriers occurs is a complex matter, although no further discussion is made in the present work, the matter is explained in section 1.6.3. Before annealing, the samples seem to have some degree of crystallinity and somewhat amorphous. These samples were deposited for 1.5 hr. As the samples are annealed at different temperatures (all for 12 hr), ranging from 1100 to 1500 °C, the cubic phase starts to form and they become completely crystalline. The monoclinic phase (as shown on 2θ of 27.5) starts to diminish as the annealing temperature increases, probably because as the temperature increases, the energy necessary to overcome the migration barrier of the atoms is reached,

thus reaching the cubic phase. Nevertheless, more diffraction peaks appear as the temperature is increased. This structural change affects all the properties, including optical, as discussed on next chapter.

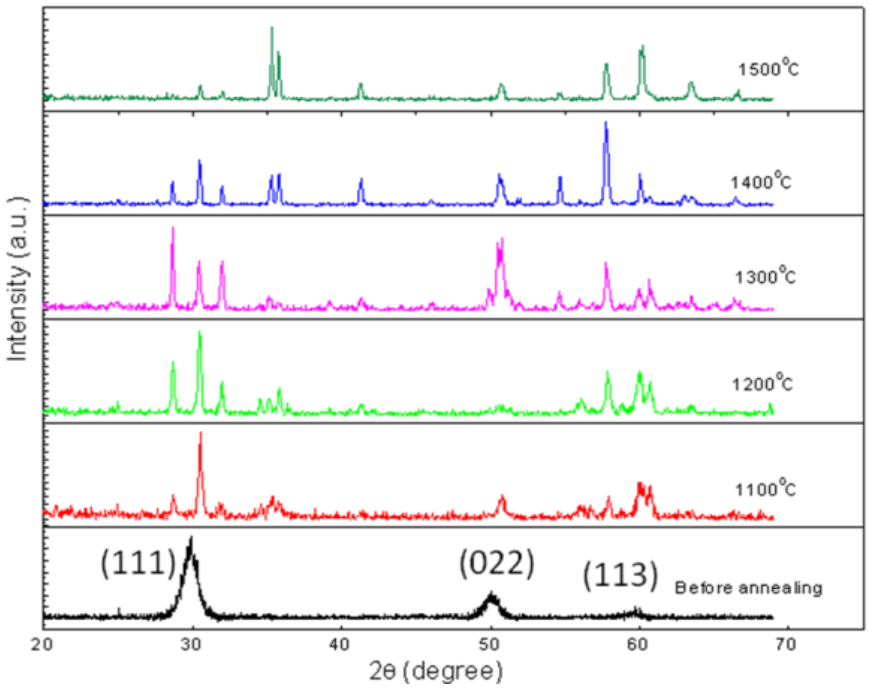

Figure 5. XRD patterns of YDH annealed samples as a function of temperature.

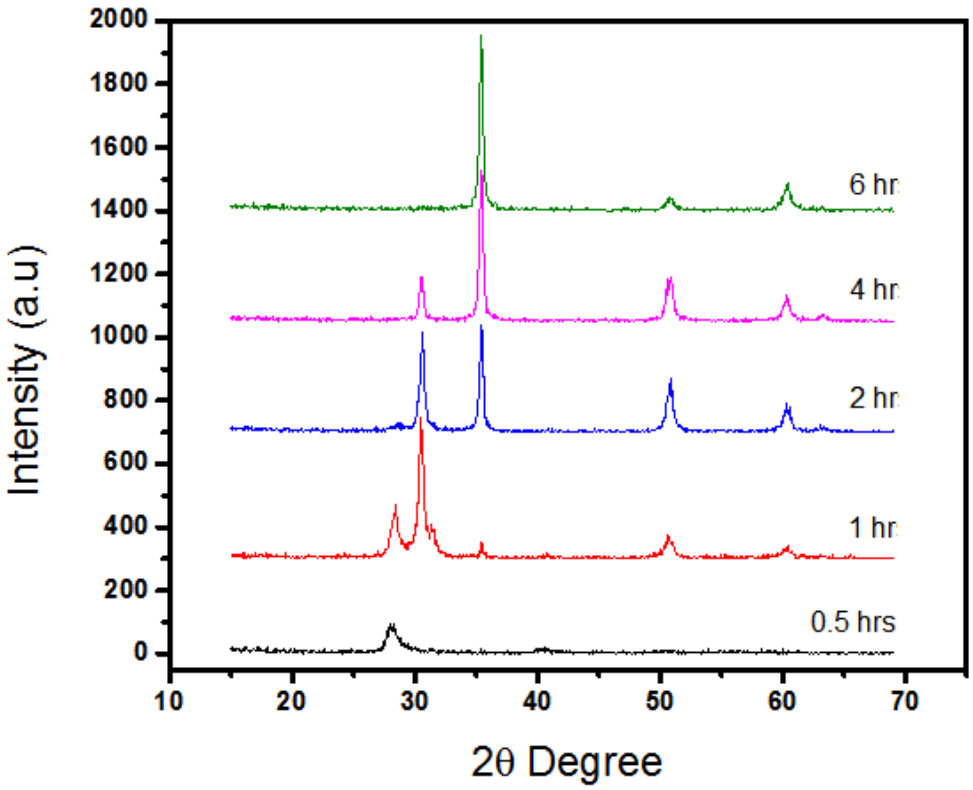

Figure 6 XRD patterns of YDH sputtered samples as a function of time.

CHAPTER 4: Optical Properties

Since the collision of a photon and an electron is similar to the collision electron-electron, the optical properties are an essential factor toward the understanding of the electronic behavior of a material. Most of the calculations performed on this work were given by the optical spectroscopy measurements.

4.1 Transmittance and absorbance spectra

The transmittance is the fraction of electromagnetic radiation traveling at a decreasing wavelength that passes through a given sample, in this case the YDH nanocrystalline thin films. The absorptivity is a logarithmic ratio between the intensity of radiation falling upon the sample and the radiation transmitted through the material. Both measurements represent the same material property, but they are inversely proportional, as defined on section 1.5.

The YDH films are mainly transparent throughout all the near IR and visible light spectrum, and high photon absorption occurs in the UV region, where the photon energy equals the optical band gap. An observation by wood et al. reports that the interference fringes shown by the YDH thin films are in function of the thickness of the samples, with the number of fringes increasing as the thickness increases [34]. In addition, in the case of the annealed samples, it is clearly seen a subtle change in the fringe pattern, indicating oxide layers and

changes in the crystal structure due to the incorporation of oxygen into the matrix.

Most of the YDH samples exhibit dichromism, a physical phenomenon that makes beams of light to split into different beams of different wavelengths, coloring the thin films in layers. This phenomenon explains the interference fringes seen in the YDH samples. For the case of YDH, the correlation between the number of interference fringes and thickness is directly proportional. This is not the case of pure hafnia, the transmittance spectra of all hafnia samples does not yield interference fringes, thus being impossible to calculate the thickness with Swanepoel's method.

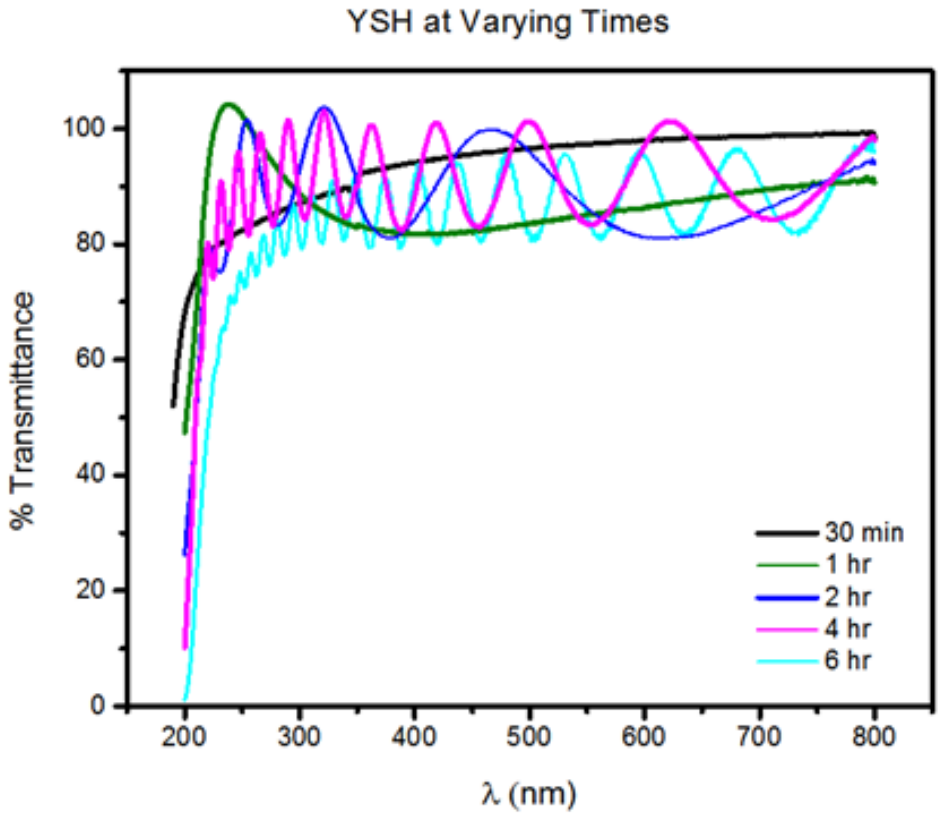

Figure 7. Transmittance spectra of samples grown at varying times

Figure 10 shows the transmission spectra of the films heated in oxygen (open air) to various temperatures and for various heating exposure times. The spectral evolution is quite different for the films. The evolution and different extent of fringe pattern for different samples is an indicative of the existence of thermal oxide grown layers with different thickness. The increasing fringe pattern trend indicates the increasing oxide thickness. The optical absorption was also measured in all these films. The data obtained are shown in Figures 11, 12 and 13. The data agree with the T% data analysis.

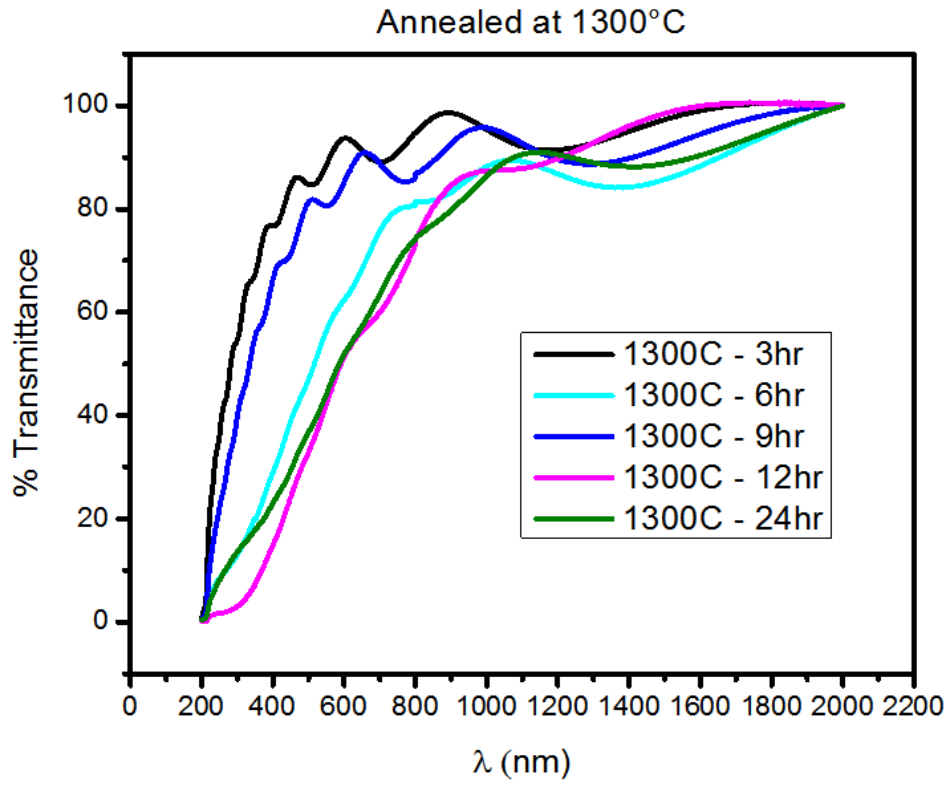

Figure 8. Transmittance spectra of samples annealed at varying times at 1300°C.

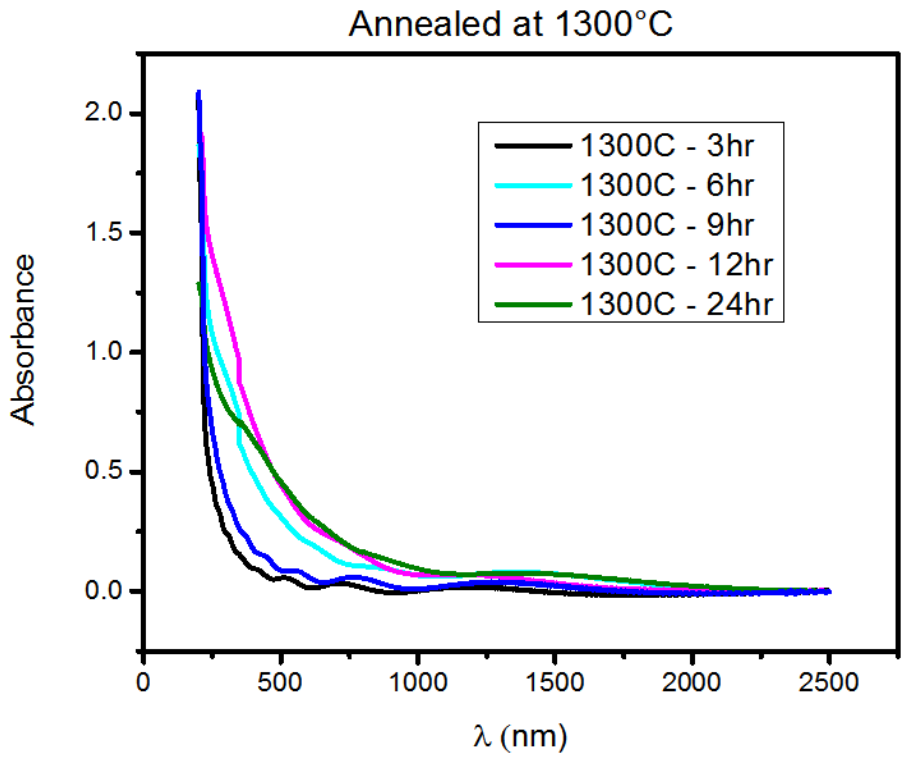

Figure 9. Absorbance spectra of samples annealed at varying times at 1300°C.

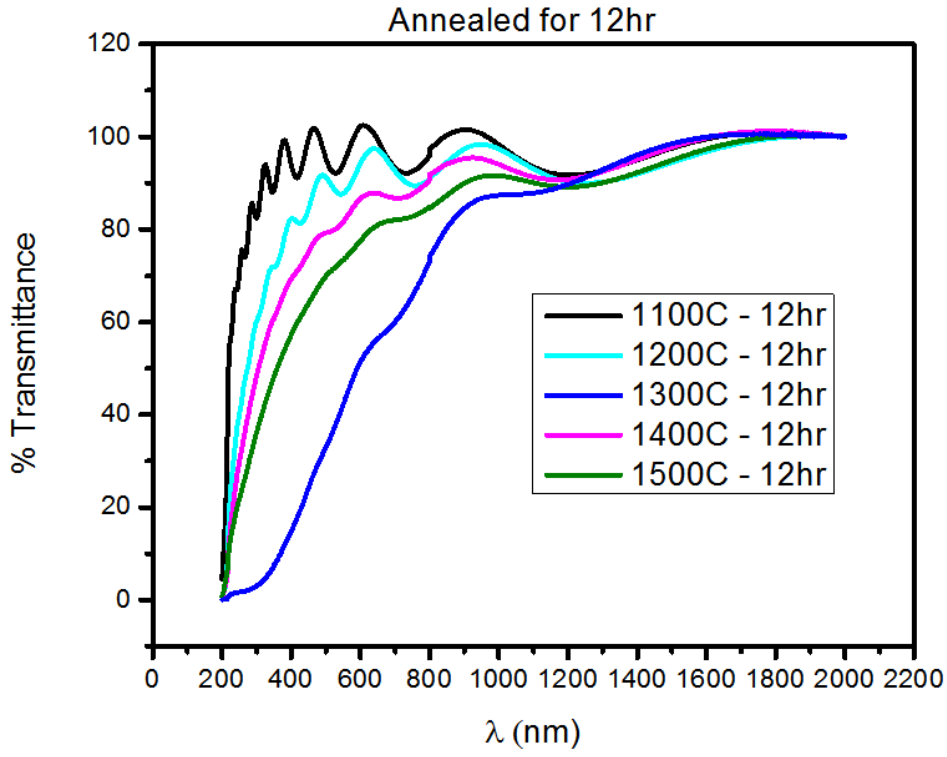

Figure 10. Transmittance spectra of samples annealed at varying temperatures for 12hr.

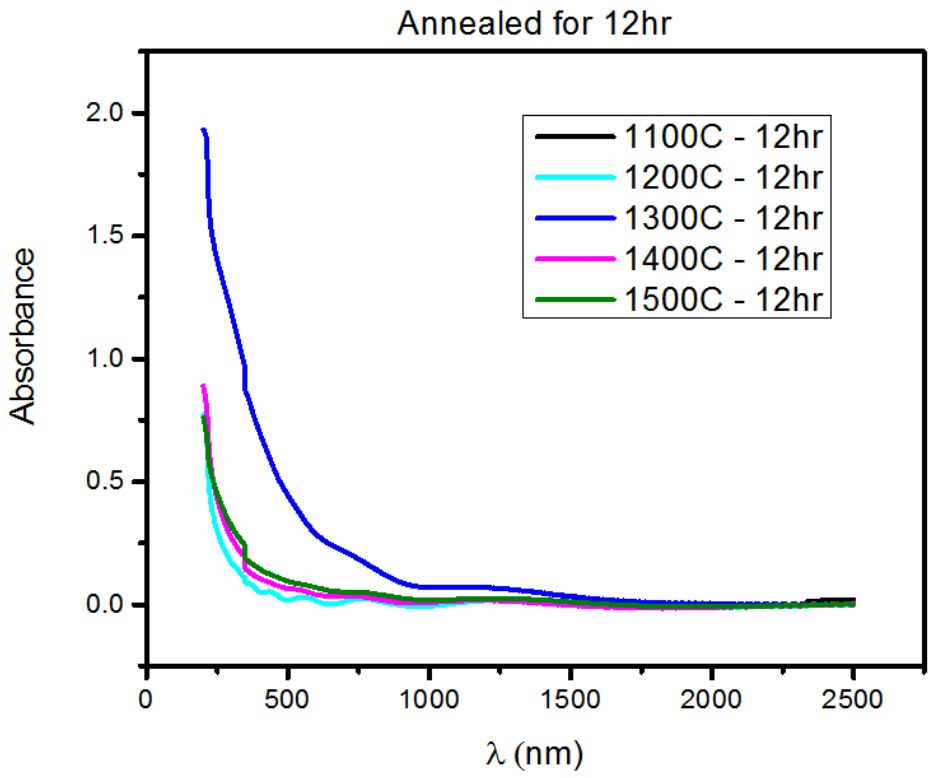

Figure 11 Absorbance spectra of samples annealed at varying temperatures for 12hr.

4.2 Absorption coefficient

The absorption coefficient, as defined on section 2.4, is the amount of light retained by the material. It is quite remarkable to the slope at the end of the absorption, where all the light gets absorbed by the material (in the Vis-UV border). This slope determines how fast the material starts absorbing the light, a steeper slope absorbs radiation faster the absorption coefficient is a good point of reference for the understanding of secondary bandgaps. It is quite clearly present in all of the annealed samples, and it also happens to be in pure hafnia.

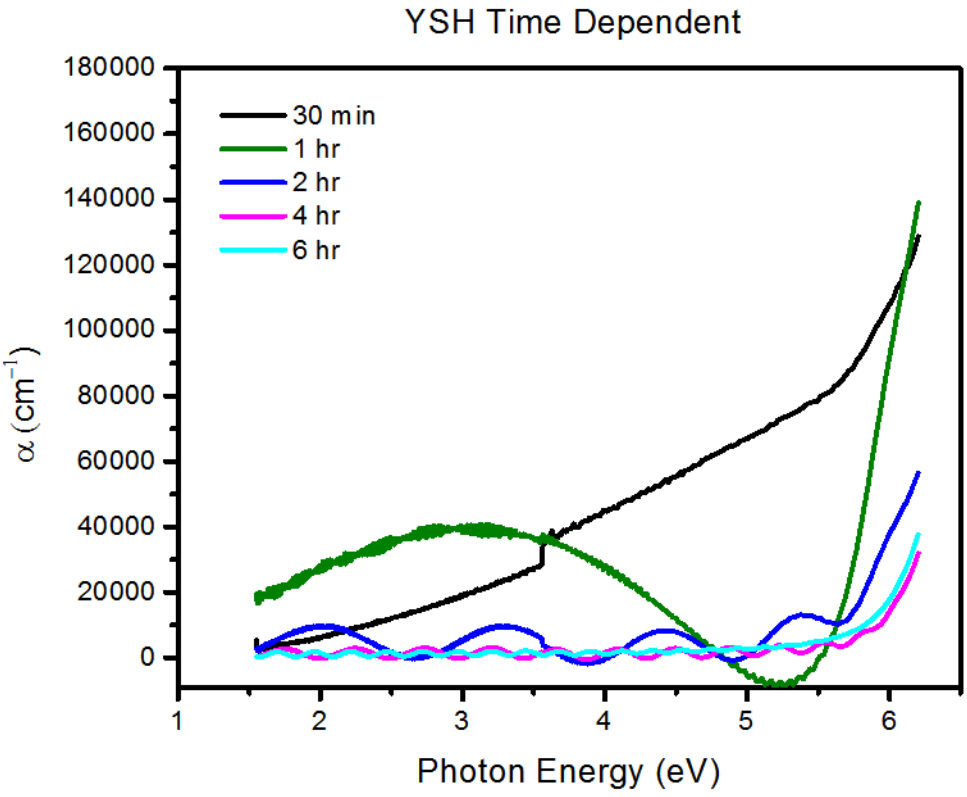

Figure 12. Absorption coefficient of samples grown varying time.

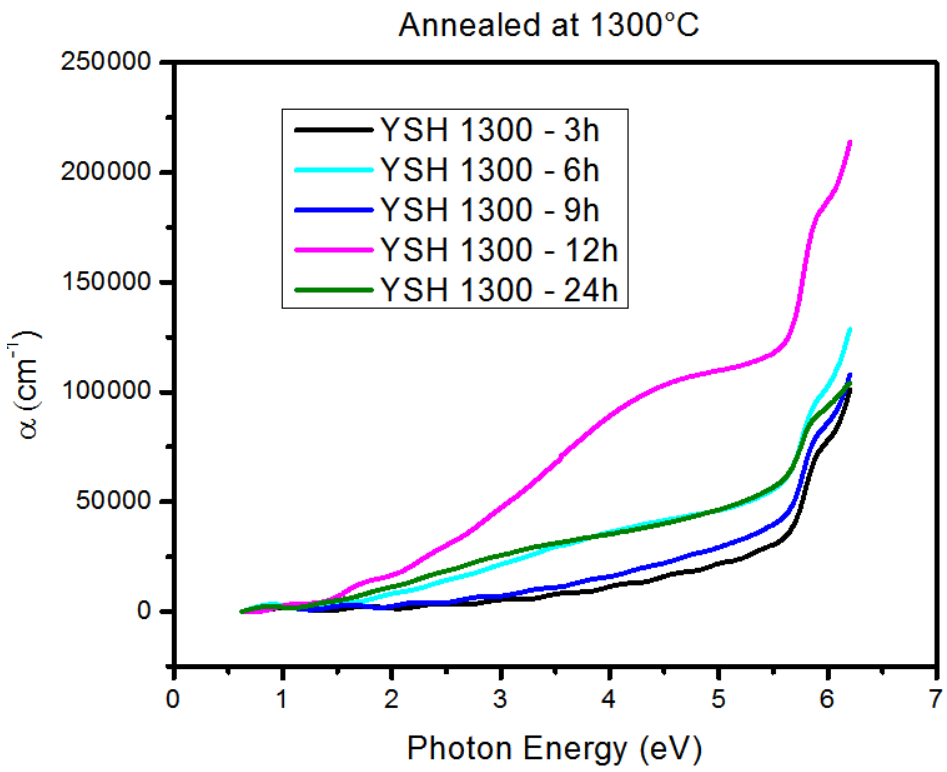

Figure 13. Absorption coefficient of samples annealed at varying times.

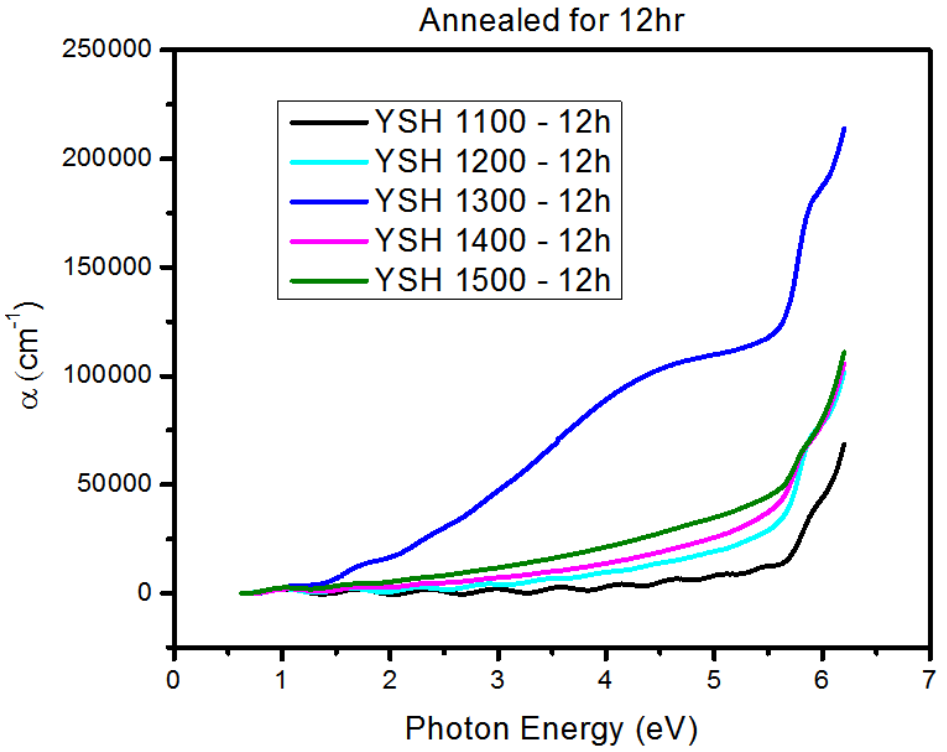

Figure 14. Absorption coefficient of annealed samples at varying temperatures.

4.3 Bandgap

Band gaps were obtained using linear regression from the $(\alpha h\nu)^2$ vs. E_p plot. As mentioned on section 1.5.2 and proved by the data, the films exhibit a direct allowed transition. The correlation between thickness and band gap can be clearly observed in figure 54 for the samples grown at variable times (30 min – 1 hr). The films exhibiting the stable cubic phase have the largest band gap (~5.9 eV), in the middle are the samples with both monoclinic and cubic phases (~5.7 eV) while the amorphous film exhibits the smallest gap (5.56 eV).

The post-deposition annealed samples, heated at variable times (3-24 hr) and constant temperature (1300 °C) exhibit a small shrinkage in their band gap as the annealing time increases. This may be attributed to the saturation of electrons in the valence band, as discussed on section1.5.2. The shrinkage ranges between 5.55 eV and 5.28 eV. A similar case is for the samples heated at variable temperatures (1100-1500 °C) for a constant time (12 hr). The shrinkage is similar in size, but these films exhibit a slightly larger gap, between 5.72 eV and 5.56 eV. In addition, all the annealed thin films exhibit secondary gaps that arise from the electrons shared by the oxygen, previously diffused into the YDH lattice product of the post-deposition annealing. According to a computational study performed by Foster et al., the oxygen is most likely incorporated in its atomic form [17]. The electrons, as explained in section 1.4.1, accommodate themselves in the oxygen vacancies caused by yttria and turn themselves into

self-trapped polarons, absorbing more photons with energies close to the UV edge. Figures 44 through 53 show all the secondary gaps. Please note that in figure 48, the secondary gap is larger than the main gap. Figures 57 and 58 show the band gap summary with the secondary gaps of the annealed samples. Even though both main and secondary gaps decrease as the annealing time increases, the secondary gap seems to reach saturation, meaning that no more oxygen is diffusing into the YDH lattice. The annealed samples at variable times seem to reach oxygen saturation, with both gaps decreasing linearly and reaching a limit.

4.3.1 Samples grown at 400°C at varying times

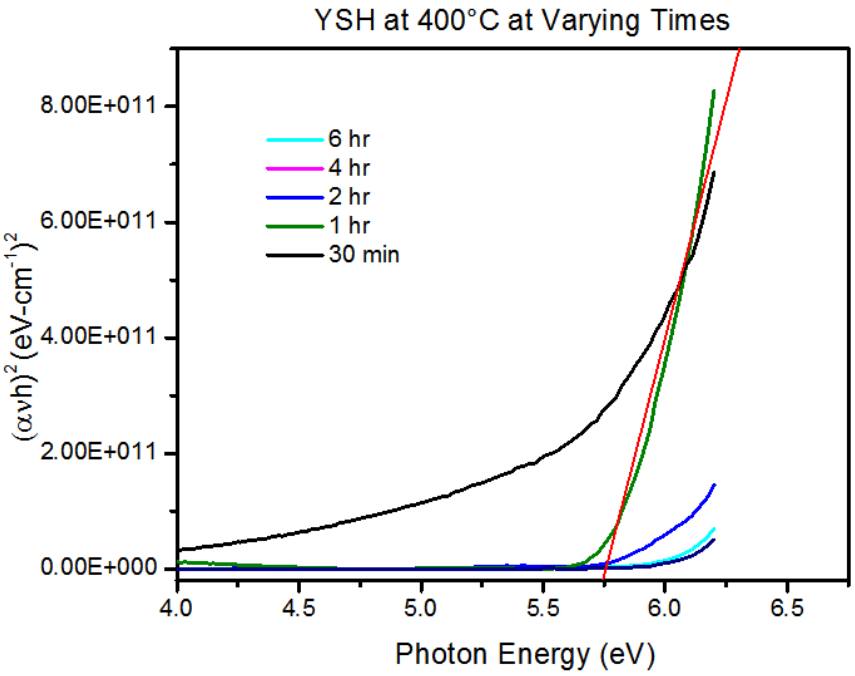

Figure 15. Bandgap of all samples grown varying times.

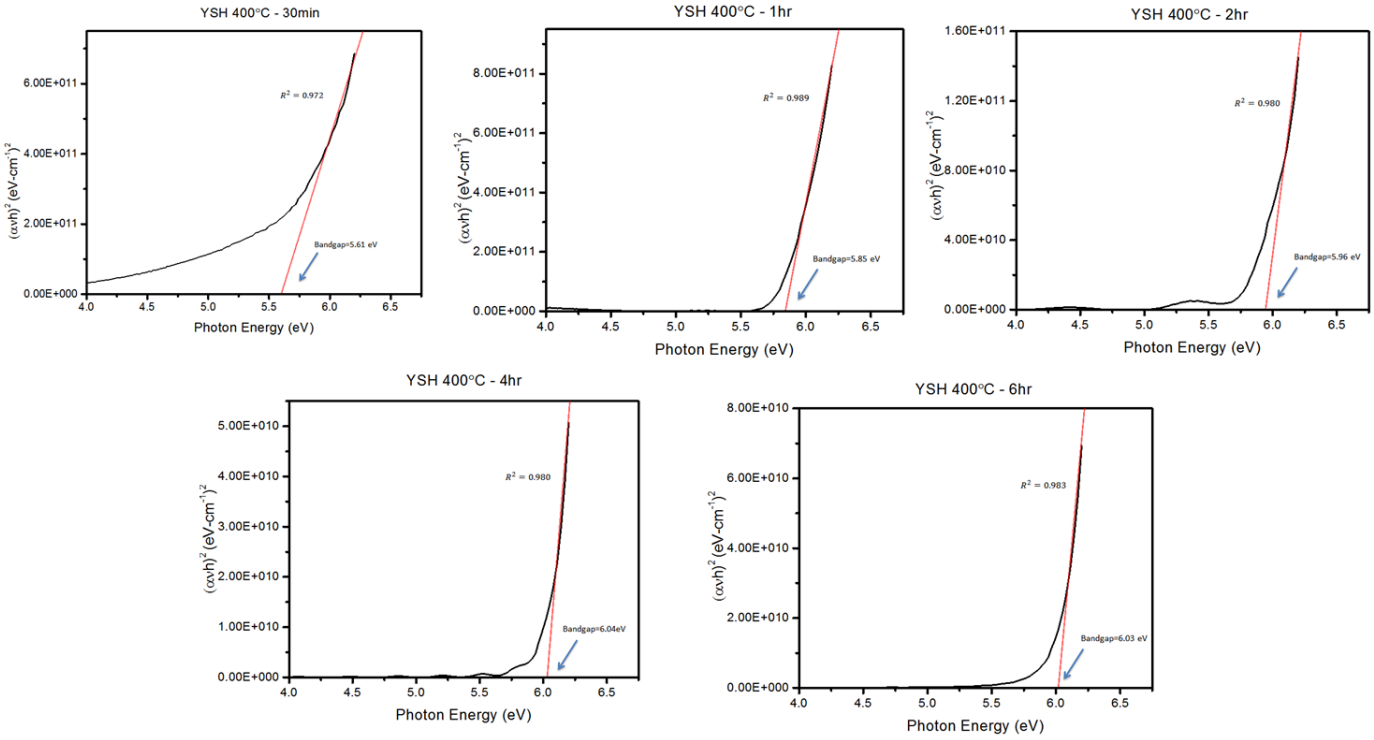

Figure 16. Bandgap of samples sputtered at 400 °C for 30 min – 6 hr

4.3.2 Samples annealed at 1300°C at varying times

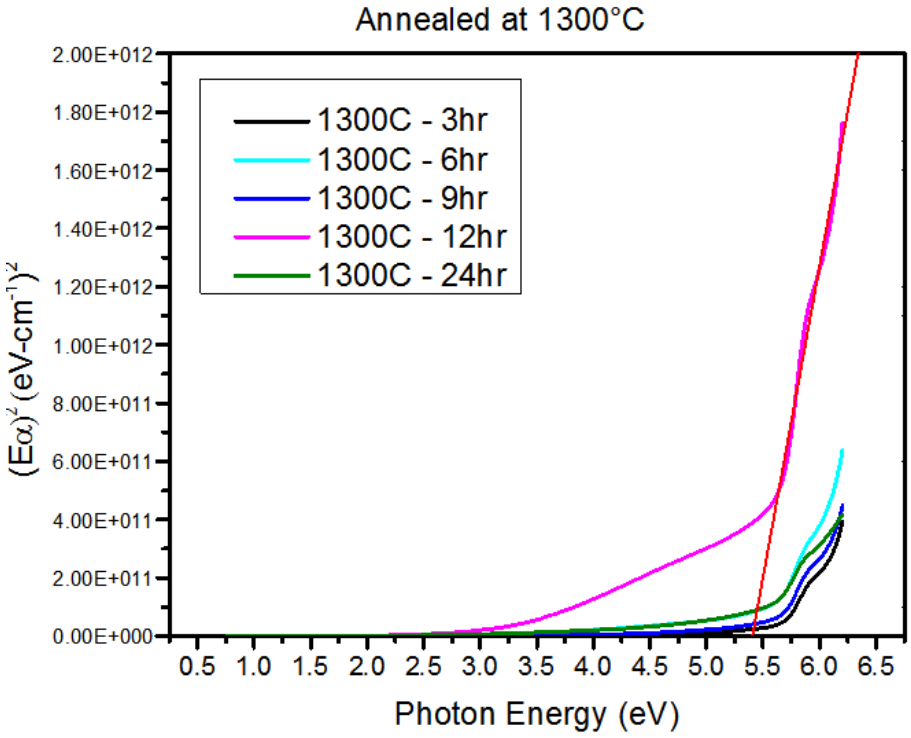

Figure 17. Bandgap of all annealed samples at varying times.

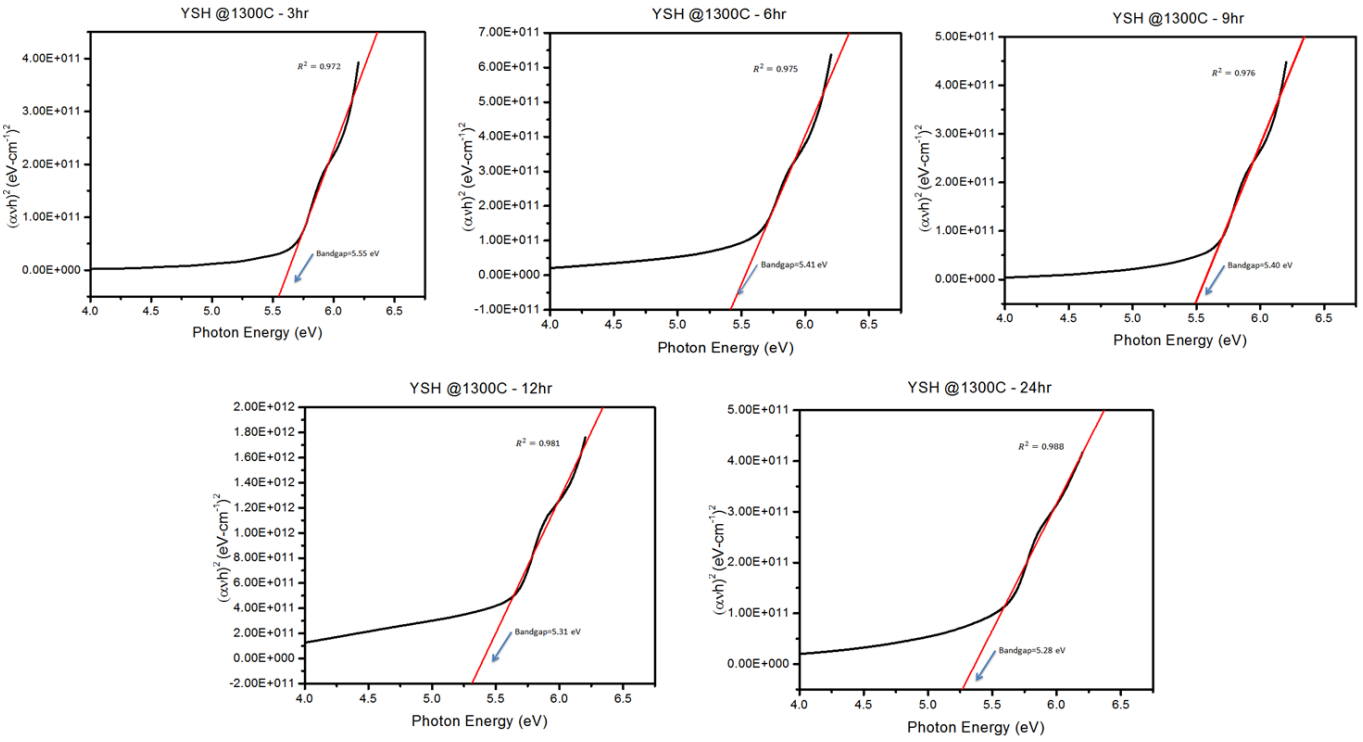

Figure 18. Bandgap of annealed at 1300 °C for 3 – 24 hours.

4.3.3 Samples annealed at varying temperatures

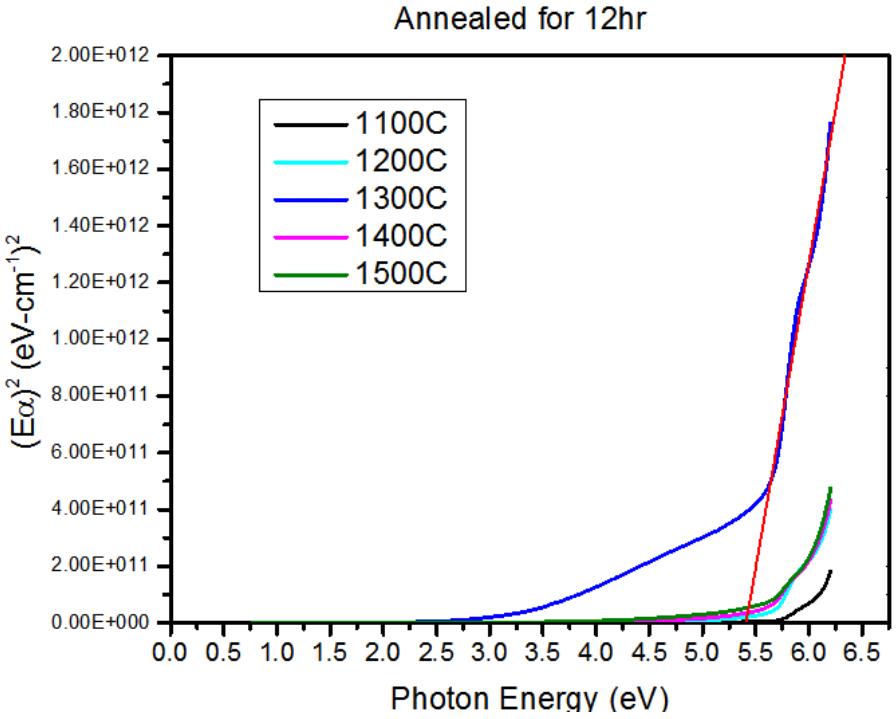

Figure 19. Bandgap of all annealed samples at varying temperatures.

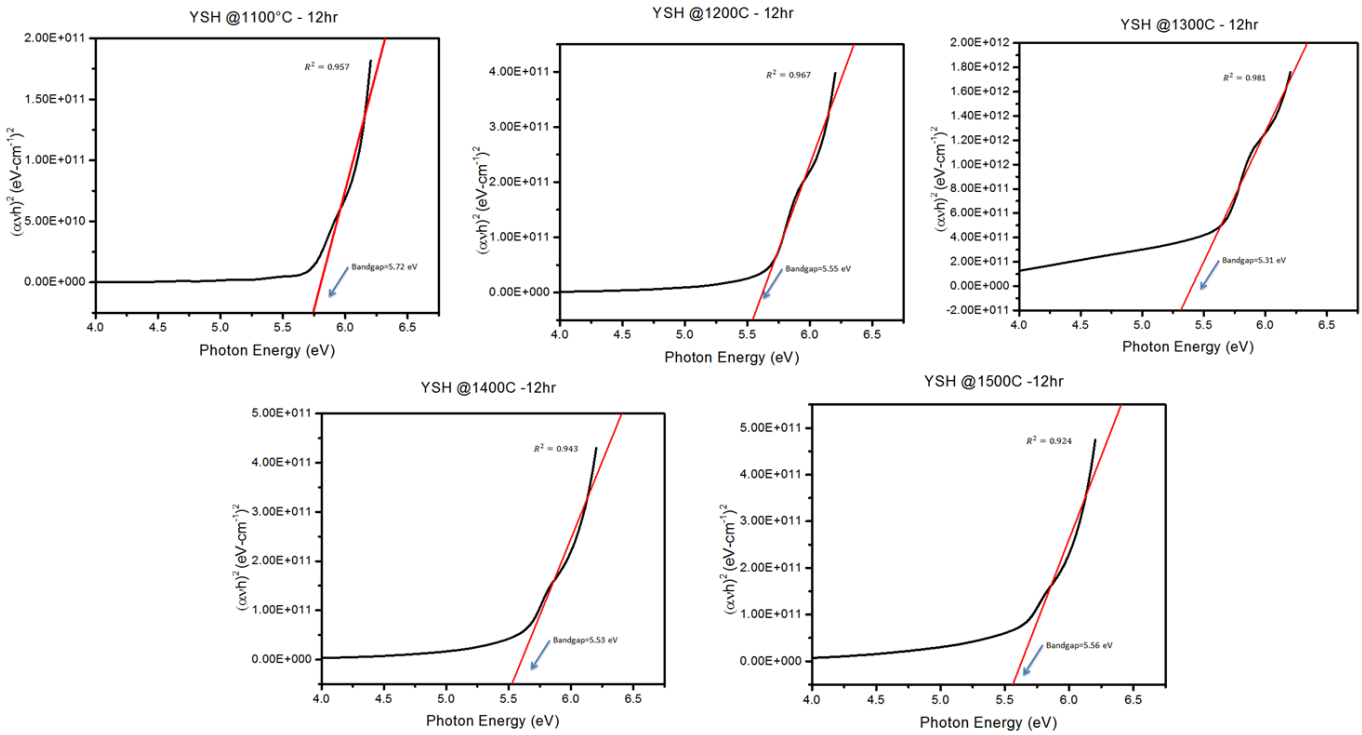

Figure 20. Bandgaps of annealed samples at 1100 °C 1500 °C for 12 hours.

4.4 Secondary gaps

4.4.1 Samples annealed at varying times

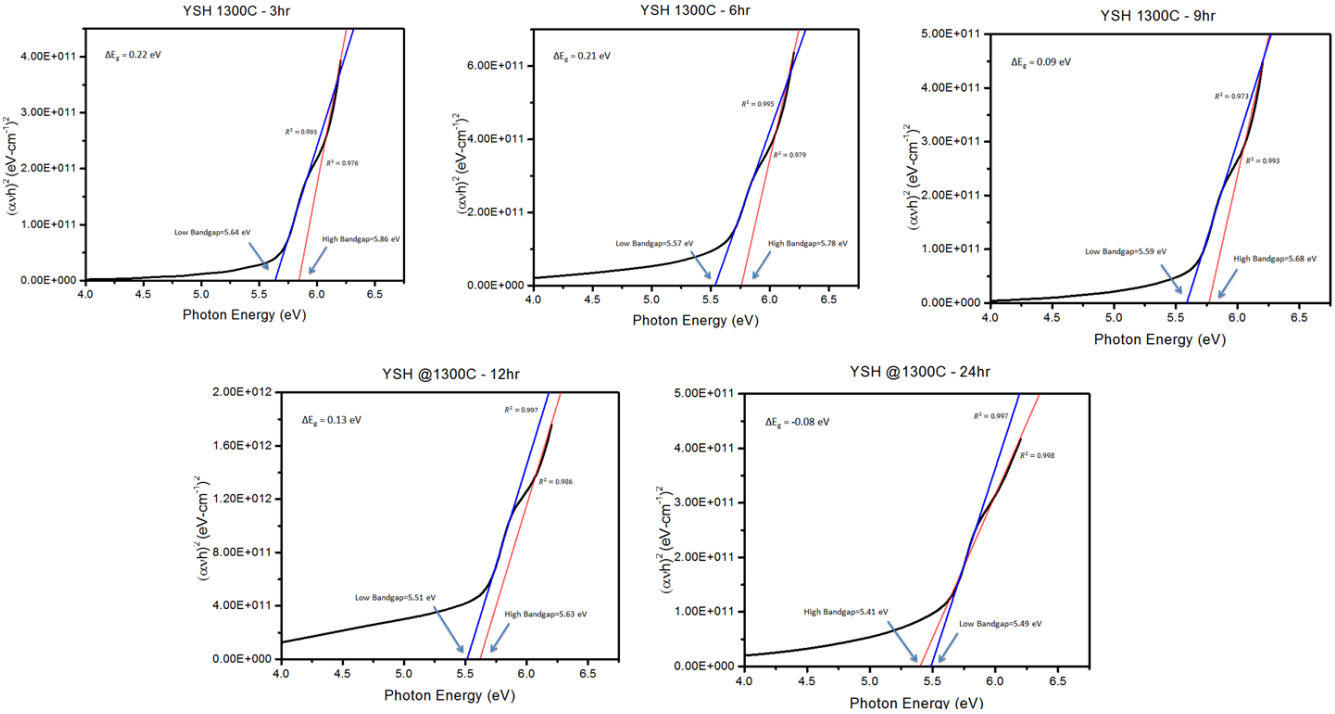

Figure 21. Main and secondary band gaps of samples annealed at 1200 °C for 3 – 24 hours.

4.4.2 Samples annealed at varying temperatures

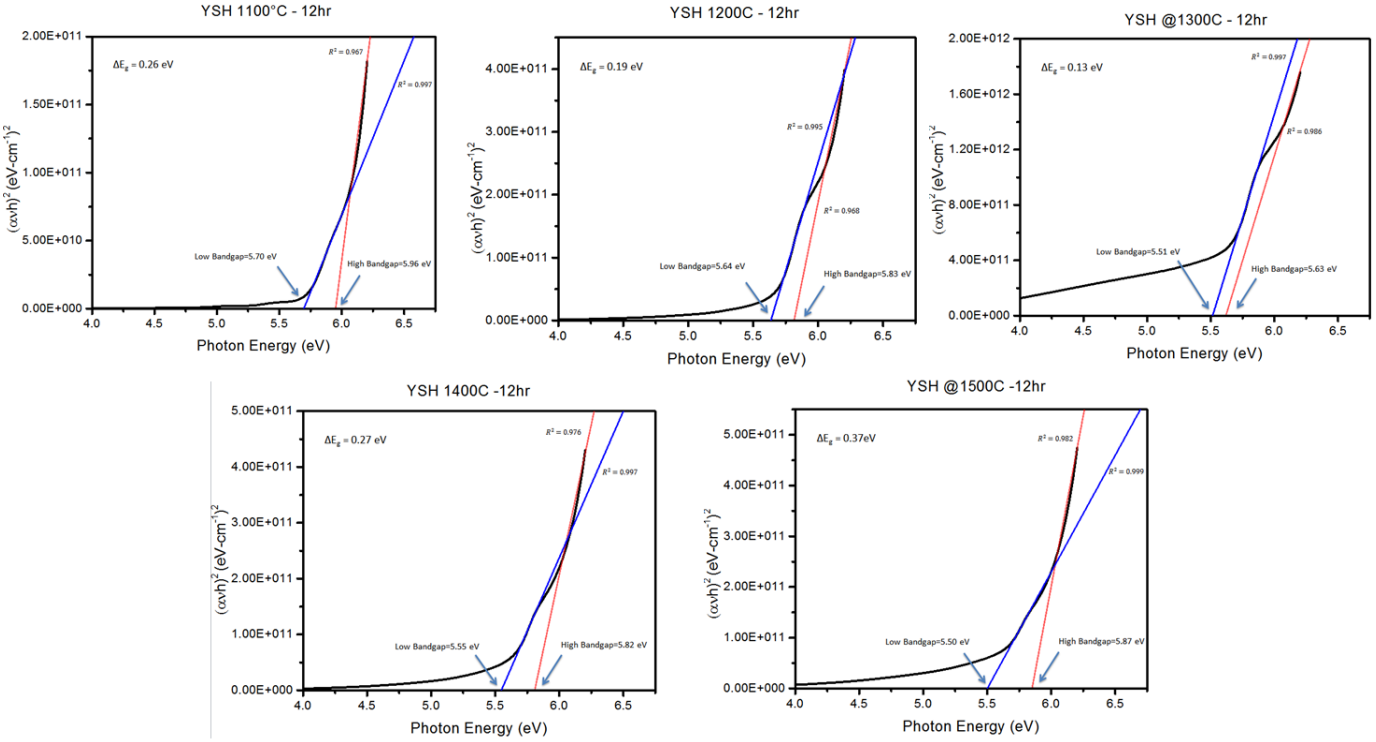

Figure 22. Main and secondary band gaps of samples annealed at 1100 °C – 1500 °C for 12 hours.

4.5 Bandgap summary

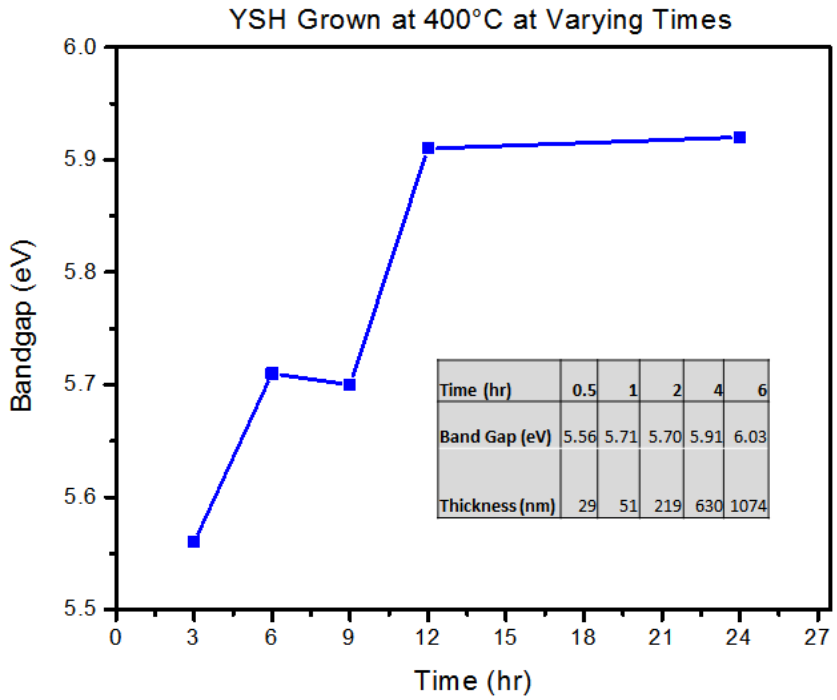

Figure 23. Bandgap, thickness and growth condition comparison for time dependent samples.

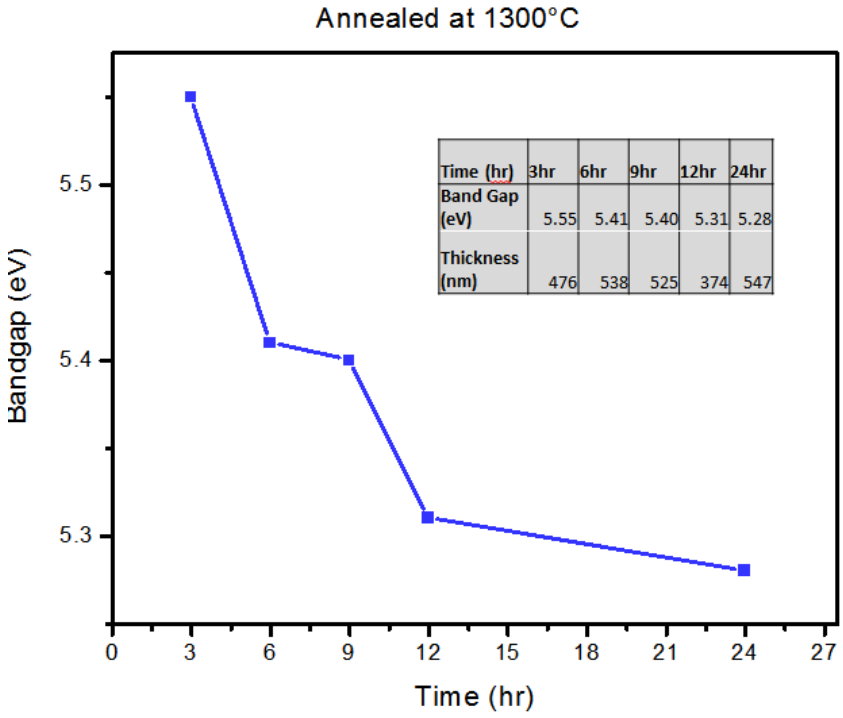

Figure 24. Bandgap, thickness and growth condition comparison for annealed samples at varying times.

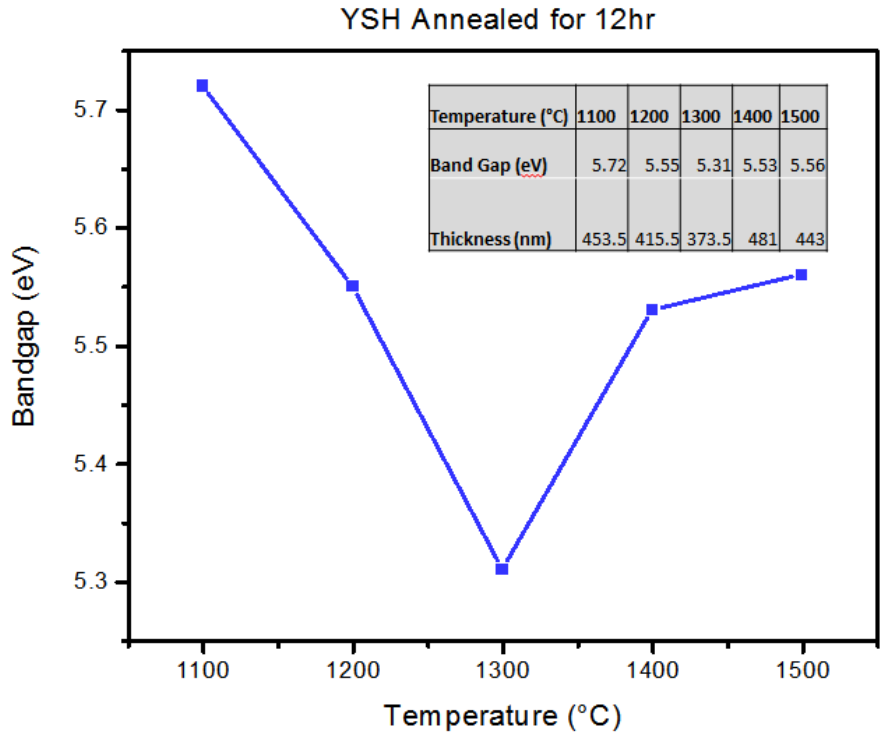

Figure 25. Bandgap, thickness and growth condition comparison for annealed samples at varying temperatures.

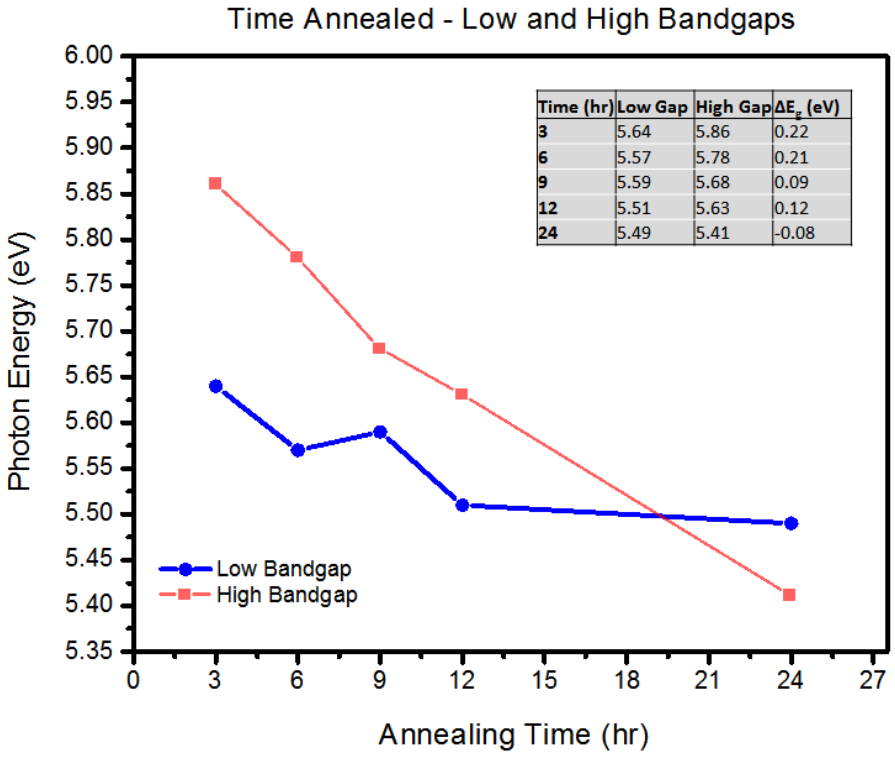

Figure 26. Bandgap, thickness and growth condition comparison for annealed samples with secondary gaps at varying times.

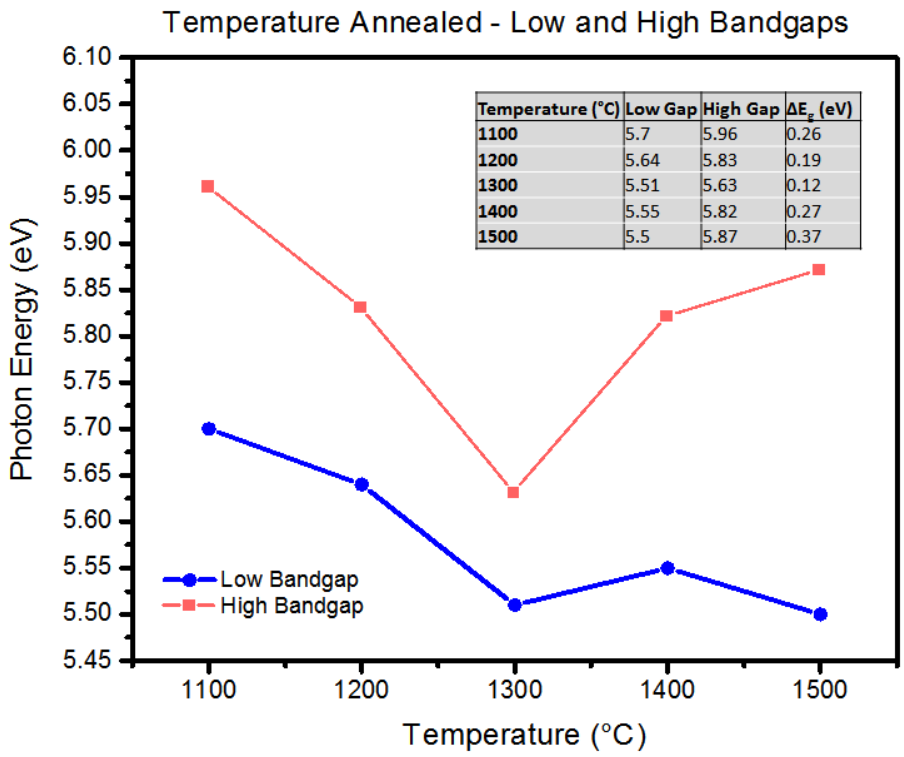

Figure 27. Bandgap, thickness and growth condition comparison for annealed samples with secondary gaps at varying times.

4.6 Index of refraction

As explained in section 1.5.3, the refractive index of a material is the ratio of the speed of light in vacuum vs the speed of light in the medium at a given radiation wavelength. As it is expected, in all the YDH samples it grows exponentially as the photon energy gets closer to UV. As the photon energy increases, radiation finds more obstacles throughout the material and it is considerably slowed down.

The samples sputtered at 400 °C for just 30 minutes (figure 59) shows a larger refractive index as compared to the rest of the samples sputtered at the same temperature for a longer period of time. Since this sample is mostly amorphous with small monoclinic crystals embedded in the matrix, it plausible that photons get absorbed and re-emitted randomly inside the film, taking a longer path. The refractive index of the rest of the films is somewhat similar, with slight variations in the high-absorption slope at around λ=230 nm. The post-deposition annealed thin films exhibit photon absorption at a much earlier stage, especially as the annealing time or temperature increases.

4.6.1 Samples grown at 400°C at varying times

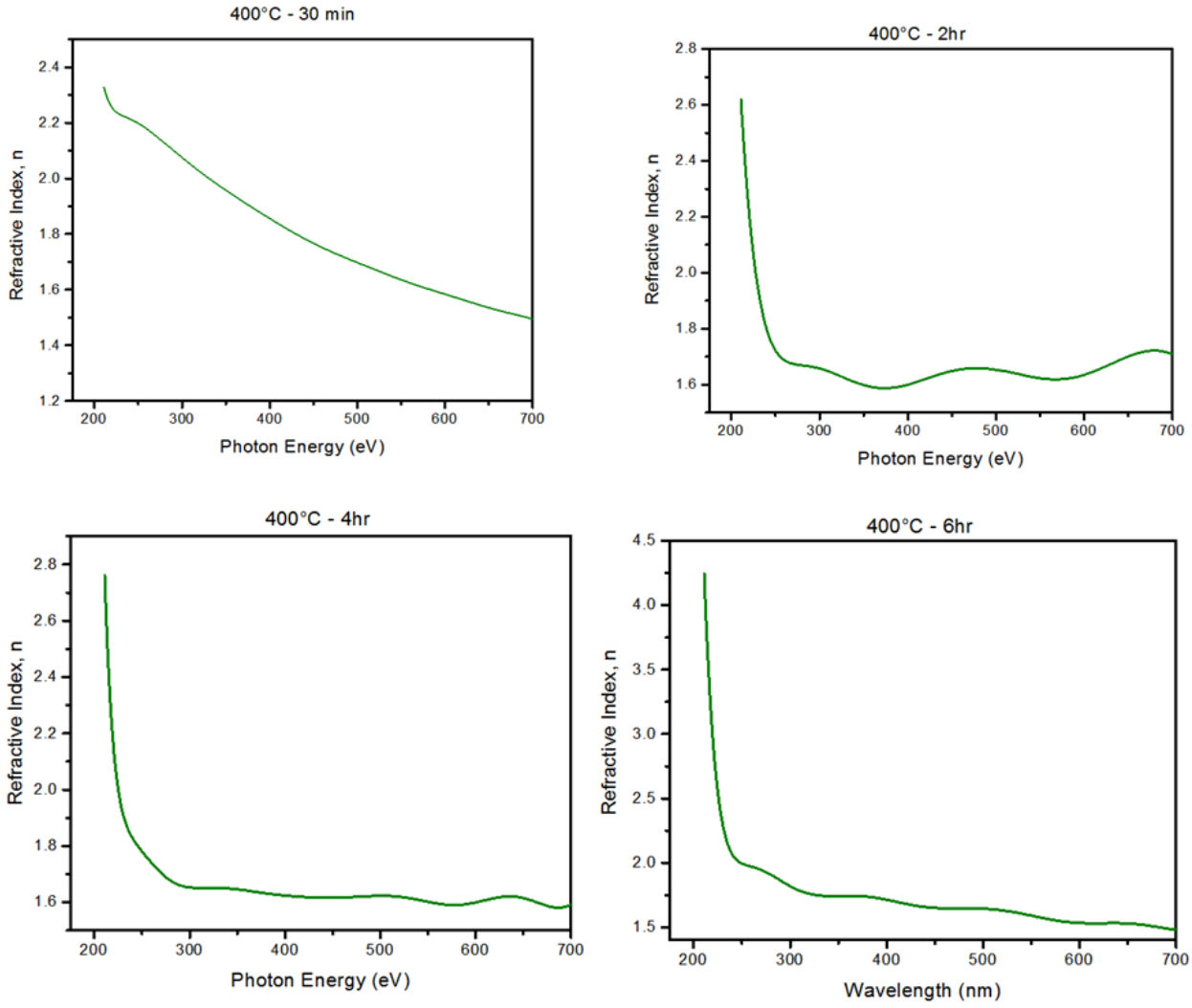

Figure 28. Refractive index of samples grown at 400 °C for 30 min – 6 hours.

4.6.2 Annealed samples at varying temperatures

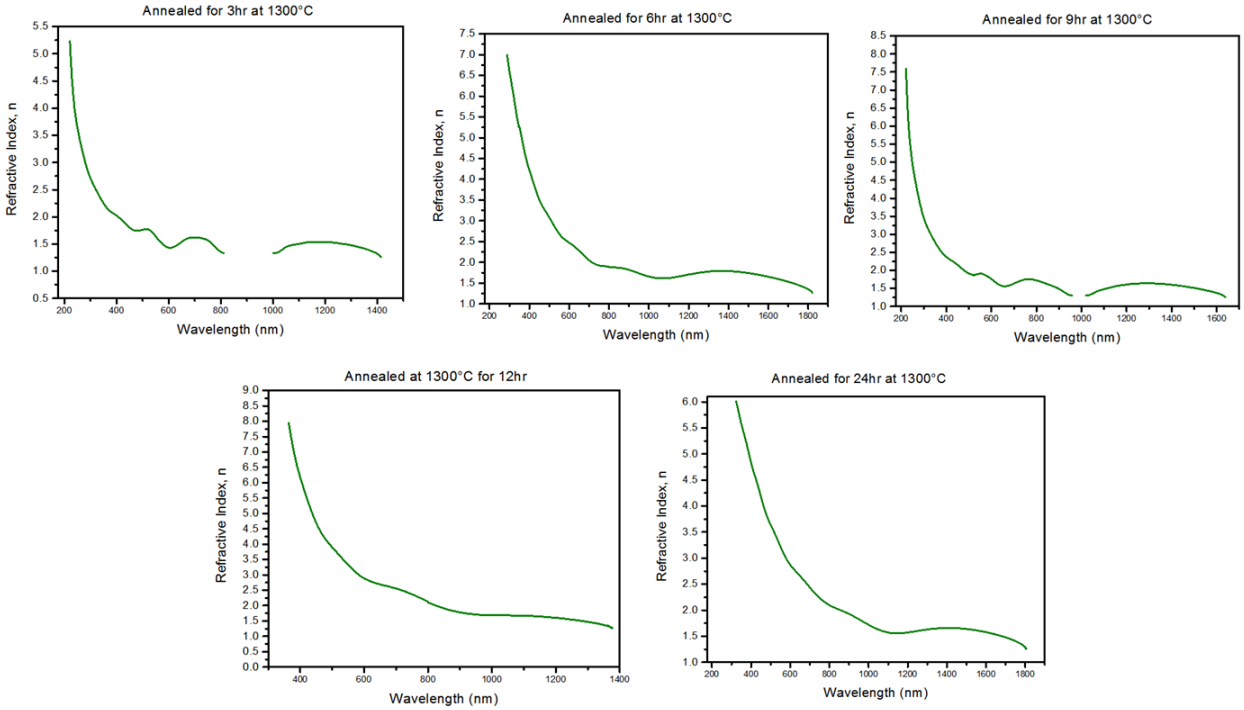

Figure 29. Refractive index of annealed samples at 1300°C for 3-24 hours.

4.6.3 Annealed samples at varying temperatures

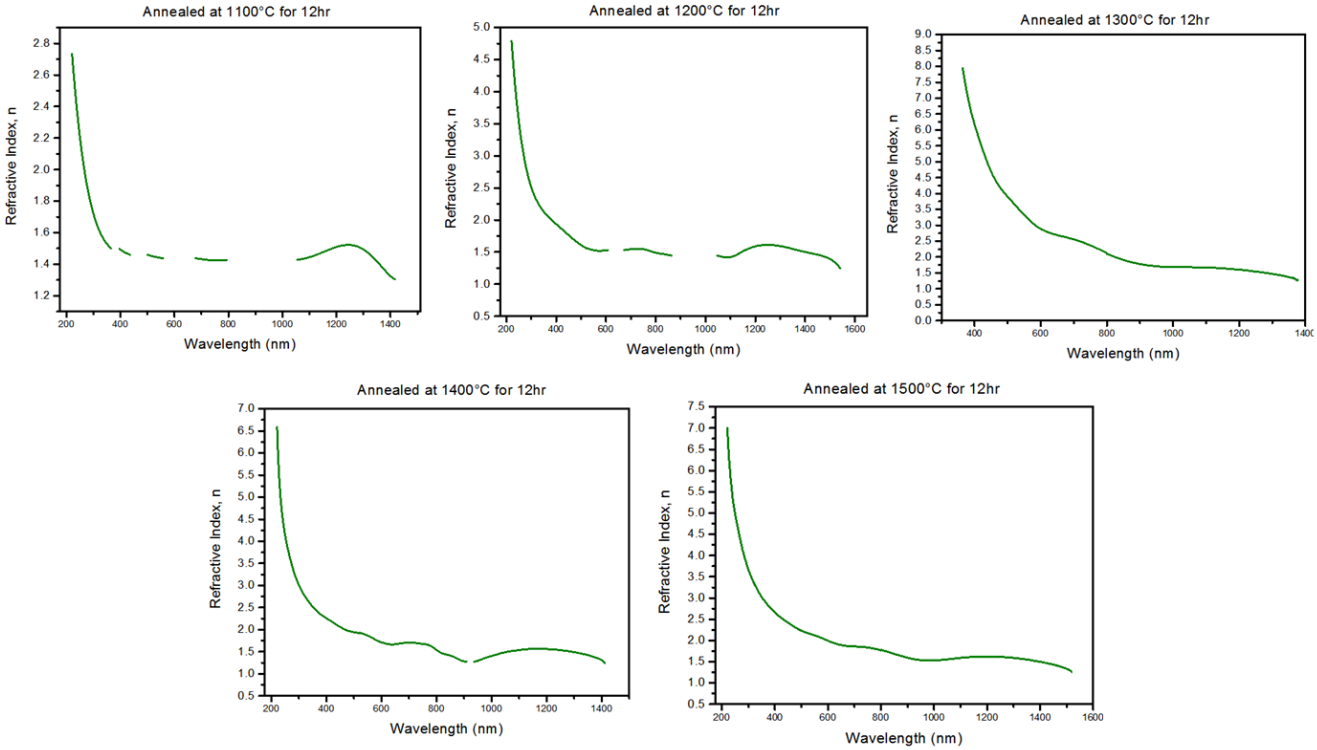

Figure 30. Refractive index of annealed samples at 1100 °C - 1500 °C for 12 hours.

References

[1] G. Moore, *Electronics*, Vol. 38, No. 8 (1965).

[2] J. D. Plummer and P. B. Griffin, *Proceedings of the IEEE* 89, 240 (2001).

[3] *International Technology Roadmap for Semiconductors*, 2002 edition, ITRS Home

Page, http://www.itrs.net/Links/2010ITRS/IRC-ITRS-MtM-v2%203.pdf (2004).

[4] A. Tohuami and A. Bouhdada, J. Appl. Phys. 89, 1880 (2001).

[5] J. Chen, T. Y. Chan, I. C. Chen, P. K. Ko and C. Hu, *IEEE Electron Device Lett*. 8, 515 (1987).

[6] S.K. Lai, *J. Appl. Phys.,* 54 (5), (1983).

[7] A. Kingon, J.P. Maria, S.K. Streiffer, *NATURE*, Vol. 406, 1032 (2000).

[8] S. Lim, S. Kriventsov, T.N. Jackson, A.M. Balbashov, R. Uecker, P. Reiche, J.L. Freeouf, G. Lucovsky, *J. Appl. Phys.*, 91 4500 (2002).

[9] W. Liu, B. Jiang, W. Zhu, *Appl. Phys. Lett.*, 77, 1047 (2000).

[10] G.D. Wilk, R.M. Wallace and J.M. Anthony, *J. Appl. Phys.*, 89, 5243 (2001).

[11] S. Ferrari, M. Modreanu, G. Scarel and M. Fancinelli, Thin Solid Films 450 (2004).

[12] S. Ferrari, M. Modreanu, G. Scarel and M. Fancinelli, Thin Solid Films 450 (2004).

[13] M. Villanueva-Ibanez, C. Le Luyer, S. Parola, O. Marty and J. Mugnier, Rev. Adv. Mater. Sci. 5 (2003).

[14] J. Tang, F. Zhang, P. Zoogman, J. Fabbri, S.-W. Chan, Y. Zhu, L.E. Brus and M.L.Steigerwald, Adv. Funct. Mater. 15 (2005)

[15] S.M. Sze, K.K. Ng, *Physics of Semiconductor Devices*, New Jersey: WILEY (2007).

[16] Fick's First Law of Diffusion, Princeton University (2012). http://www.princeton.edu/~achaney/tmve/wiki100k/docs/Fick_s_law_of_diffusion.html

[17] A.S. Foster, A.L. Shluger, R.M. Nieminen, *Phys. Rev. Lett.*, Vol. 89 No. 22 (2002).

[18] B.W. Busch, W.H. Schulte, E. Garfunkel, T. Gustafsson, W. Qi, R. Nieh, J. Lee, *Phys. Rev. B*, 62 R 13290 (2000).

[19] U. Brossman, R. Wurschum, U. Sodervall, H.E. Schaefer, *J. Appl. Phys*, 85, 7656 (1999).

[20] Pacchioni, G., Valerei, S., "Oxide Ultrathin films", Wiley-Vch, 2012. ISBN 978-3-527-33016-4.

[21] J. X. Zheng, G. Ceder, T. Maxisch, W. K. Chim and W. K. Choi, *Phys. Rev. B*, 75 104112 (2007).

[22] D. Muñoz Ramos, J. L. Gavartin, and A. L. Shluger, *Phys. Rev. B*, 75 205336 (2007).

[23] P. Broqvist and A. Pasquarello, Appl. Phys. Lett. 89, 262904 (2006).

[24] J.L. Gavartin, A.L. Shluger, *J. Appl. Phys.*, 97, 053704 (2005).

[25] D.B. Holt and G. Yacobi, "Extended Defects in Semiconductors", Cambridge

[26] Helmut Foll, "Defects in Crystals", Germany (2011).

[27] M. Houssa, "High-k Gate Dielectrics", IoP, Bristol and Philadelphia (2004).

[28] G.D. Wilk, R.M. Wallace and J.M. Anthony, *J. Appl. Phys.*, 87 484 (2000).

[29] G.D. Wilk, R.M. Wallace and J.M. Anthony, *J. Appl. Phys.*, 89 5243 (2001).

[30] M.F. Al-Kuhaili, *Opt. Matls.*, 27 385 (2004).

[31] X. Chen, L. Song, L. You and L. Zhao, *App. Sur. Sci.*, In press, (2013).

[32] R. Swanepoel, *J. Phys. E.: Sci. Instrum.*, Vol. 16 (1983).

[33] R. Swanepoel, *J. Opt. Soc. Am. A.*, Vol. 2, No. 8 (1985).

[34] D.L. Wood, K. Nassau, T.Y. Kometani and D.L. Nash, *App. Optics*, 29 604 (1990).

[35] F.W. Sears, M.W. Zemansky and H.D. Young, *University Physics* 6th ed., ISBN 0-201-07199-1

[36] B.G. Yacobi, *Semiconductor Materials*, Microdevices, ISBN 0-306-47361-5 (2003).

[37] R., Nave. *Semiconductor Band Gaps*. Georgia State University (July 2013). http://hyperphysics.phy-astr.gsu.edu/hbase/tables/semgap.html

[38] R., Nave. *Dielectric Constants*. Georgia State University (July 2013). http://hyperphysics.phy-astr.gsu.edu/hbase/tables/diel.html

[39] Thelen Tree Farm, *Tech Data*, (July 2013). http://thelen.us/1dielectric.php

[40] Vega, *Dielectric Constant List*, (July 2013). http://www.ohmartvega.com/downloads/forms-certificates/dielectric_constants_list.pdf

[41] Clipper Controls, *Dielectric Constant Values*, (July 2013). http://www.clippercontrols.com/pages/dielectric-constant-values.html

[42] Varec Tank Gauging, *Dielectric Constants*, (July 2013). http://www.tankgauging.com/applications/dielectricconstants.html

[43] Filmetrics, *Refractive Index Database*, (July 2013). http://www.filmetrics.com/refractive-index-database

[44] W. H. Strehlow, L. E. Cook. *J. Phys. Chem. Ref. Data,* Vol. 2 No.1. (1973).

[45] Marvin J. Weber. *Refractive Index Database (2003).* http://refractiveindex.info/

[46] H. Kim, C.M. Gilmore, A. Pique, J.S. Horwitz, H. Mattoussi, *J. Appl. Phys.,* 86, 6451 (1999).

[47] The Engineering ToolBox. *Thermal Conductivity of Common Materials.* http://engineeringtoolbox.com/thermal-conductivity-d_429.html

[48] Pixel and Poly. *Index of Refraction Values* (2011). http://www.pixelandpoly.com/ior.html

[49] M. Noor-A-Alam, C.V. Ramana, *Ceramics International,* 38, 2957-2961 (2012).

[50] Thermal Evaporation, *WO_3 Properties* (May 2010). http://www.thermal-evaporation.com/oxide/wo3.html

[51] Stierle, A., Kasper, N., Dosch, C., Borg, M., Andersen, J., De Santis, M., Gauthier, Y., Konvicka, C., Schmid, M., and Varga, P., *Phys. Rev. Lett., 88, 246103 (2002).*

[52] University of Cambridge, *Direct and Indirect Band Gap Semiconductors* (2013). http://www.doitpoms.ac.uk/tlplib/semiconductors/direct.php

[53] University of Cambridge, *Charge Carriers in Semiconductors* (2013). www.doitpoms.ac.uk/tlplib/semiconductors/charge_carriers.php

[54] University of Glasgow, *Charge Collection in GaAs Detectors* (1997). http://ppewww.physics.gla.ac.uk/preprints/97/05/psd1/psd1.html

[55] Belle Dume. *Leds Move into Ultra Violet,* Physics World (May 2006). http://physicsworld.com/cws/article/news/2006/may/17/leds-move-into-the-ultraviolet

[56] C.V. Ramana, K. Kamala Bharathi, A. Garcia, A.L. Campbell, A.L., *J. Phys. Chem.,* C 116 9955 (2012).

[57] M. Noor-A-Alam, K. Abhilash, C.V. Ramana, *Thin Solid Films*, 520 6631 (2012).

[58] http://pubs.rsc.org/en/content/articlehtml/2005/jm/b417143h

[59] L. Shei, Y. Zhou, J. Yin, Z. Liu, *J. Appl. Phys.*, 107 014104 (2010).

[60] K. Kita, K. Kyuno, A. Toriumi, *Appl. Phys. Let.,* 86 102906 (2005).

[61] M. Villanueva-Ibañez, C. Le Luyer, O. Marty, J. Mugnier, *Opt. Mater.*, 24 51(2003).

[62] Koji Kita, Kentaro Kyuno, Akira Toriumi, App. Phys. Lett., 86 102906 (2005).

[63] X. Zhao and D. Vanderbilt, Phys. Rev. B 65, 233106 (2002).

[64] Hadis Morkoç *Nitride Semiconductor Devices, p. 197,* ISBN: 978-3-527-41101-6 (2013).

[65] R. Terki, G. Bertrand, H. Aourag, C. Coddet, Mat. Lett., 62 1484–1486 (2008).

[66] Intel Corp., News Room (2013).

http://www.intel.com/content/www/us/en/quality/quality-manufacturing-process.html

[67] Evgeni Gusev, *Defects in High-k Gate Dielectric Stacksi*, p. 110, ISBN: 978-1-4020-4366-6 (2006).

[68] E.J. Rubio, G. Martinez, M. Noor-A-Alama, S.W. Staffordb, V. Shutthanandan, C.V. Ramana, Surf. & Coatings Tech., in press (2013).

[69] Encyclopedia Britannica, Inc. (2013).

http://www.britannica.com/EBchecked/topic/656482/Zener-effect

Curriculum Vitae • Alejandro Ortega

Education

Alex Ortega obtained his bachelor's degree (2011) in Mechanical Engineering from The University of Texas at El Paso, and it is currently finishing his master of science in Metallurgical & Materials Engineering (2013), with an overall GPA of 3.71. In addition, he spent one semester studying abroad in Czech Technical University of Prague, in the Czech Republic (2010).

Research Experience

Alex Ortega worked as a research assistant in the chemistry supramolecular laboratory of Dr. J.C. Noveron in two occasions: first in 2007 for two years creating molecular dynamic simulations for the lab's chemical models, and in 2010 doing compound synthesis, extraction, crystallization and characterization.

In 2011, he obtained a research assistant position in the cSETR laboratory with Dr. C.V. Ramana, doing thin film growth, characterization and the preparation of technical reports.

Teaching Experience

His teaching experience includes working as a peer leader for the mathematics department of UTEP for a year and a half.

Extra-Curricular Activities

Alex Ortega has been through several extra-curricular activities, but the principal include: Miner Trotter (student exchange organization in El Paso): he first served as the cofounder and vice-president of external affairs (2010), then as the president of the organization (2011) and now he serves as an adviser and coordinator.

Academic Achievements

He has been to two conferences: ICMCTF in San Diego (2013) presenting a published paper who shares the same name: "Correlation between phase and optical properties of yttrium-doped hafnium oxide nanocrystalline thin films". Second conference was SWTCC in El Paso (2009) presenting "Study of hydrophobic effect on metal-organic materials using CHARM++".

Skills

Some of his personal skills include bilingual proficiency in English and Spanish, as well as biculturalism; excellent team building and relationship management skills; problem solving/decision making; cultural exchange and adaptation.

His academic skills include: proficiency in thin films, semiconductors, protective coatings, materials characterization, materials properties, mechanical behavior, alloy heat treatment, material selection, among others.

His computing skills include CAD modeling, FEA, molecular dynamics, HVAC modeling, MS office, OriginLab, Mathematica, Matlab, Adobe Photoshop, Flash, Fireworks and Dreamweaver, Corel Draw and Linux.